The Abdus Salam
International Centre for Theoretical Physics

United Nations
Educational, Scientific and
Cultural Organization

IAEA
International Atomic Energy Agency

1936-34

Advanced School on Synchrotron and Free Electron Laser Sources and their Multidisciplinary Applications

7 - 25 April 2008

Atomic-Level Characterization of Materials with Core- and Valence-Level Photoemission: Basic Phenomena and Future Directions

Charles S. Fadley
Materials Sciences Division,
Lawrence Berkeley National Laboratory
Berkeley
CA 94720 USA

Corrected

Submitted to Surface and Interface Analysis as part of the
Proceedings of the Sixth International Symposium on Atomic-Level Characterizations of New Materials and Devices, Kanazawa, Japan, 2007

Atomic-Level Characterization of Materials with Core- and Valence-Level Photoemission: Basic Phenomena and Future Directions

Charles S. Fadley
Department of Physics, University of California Davis, Davis, CA 95616 USA
Materials Sciences Division, Lawrence Berkeley National Laboratory, Berkeley, CA 94720 USA
During 2006-2007:
Institute for Solid State Research, IFF-9, Jűlich Research Center, Jűlich, D-52425 Germany
Hasylab, University of Hamburg, Hamburg, D-22761 Germany

Summary

In this overview, the basic concepts of core and valence photoelectron spectroscopy (photoemission), photoelectron diffraction, and photoelectron holography are introduced. Then some current developments in these techniques that should enhance their utility for atomic-level characterization of new materials and surface chemical processes are discussed, including measurements with hard x-ray excitation, standing-wave excitation, and ambient pressures in the multi-torr regime.

1 Basic Phenomena and Experiments

Photoelectron spectroscopy, often referred to simply as photoemission, has its fundamental origin in the photoelectric effect, which was first explained by Einstein in 1905 [1] , led to a Nobel Prize for him in 1921, and was key to the later development of the concept of the photon as the quantum of electromagnetic energy. In the period since the late 1950s, the photoelectric effect has been developed into one of the most powerful tools for studying the composition and electronic structure of matter. K. Siegbahn received the Nobel Prize for the further development of several aspects of photoelectron spectroscopy in 1981 [2].

As currently used, the fundamental energy conservation equation is the following [3,4]:

$$h\nu = E_{binding}^{Vacuum} + E_{kinetic}^{'} = E_{binding}^{Fermi} + \varphi_{spectrometer} + E_{kinetic} \qquad (1)$$

in which h is Planck's constant; ν is the photon frequency; $E_{binding}^{Vacuum}$ is the binding energy of a given electron relative to the vacuum level of the sample; $E_{kinetic}^{'}$ is the kinetic energy of the emitted electron just as it leaves the sample; $E_{kinetic}$ is the kinetic energy as measured finally in the spectrometer, and may be different from $E_{kinetic}^{'}$ by a small contact potential difference if the sample is a solid; $E_{binding}^{Fermi}$ is the binding energy relative to the Fermi level or electron chemical potential; and $\varphi_{spectrometer}$ is the work function of the spectrometer used to measure

kinetic energy. In very precise measurements, and/or as the excitation energy is increased into the multi-keV regime, both kinetic energies may be reduced by a recoil energy E_{recoil} given to the sample due to momentum conservation; this we discuss below in connection with hard x-ray photoemission. If one measures the electron kinetic energy, and perhaps also knows the spectrometer work function, it is thus possible to measure the binding energies of various inner (or core) electrons, as well as those of the outer (or valence) electrons that are involved in chemical bonding. Such measurements reveal a broad array of phenomena that can be used to characterize a given material, in particular the near-surface regions of solids from which most photoelectrons are emitted. Photoemission is also very fruitfully applied to gas-phase atoms, molecules, and clusters, but we will here focus on work on solid samples.

It is also useful to specify the binding energy more precisely from the point of view of theoretical calculations, and we can write this as:

$$E_{binding}^{Vacuum}(Qn\ell j,K) = E_{final}(N-1,Qn\ell\ j\ hole,K) - E_{initial}(N)\ , \qquad (2)$$

where we for simplicity consider a binding energy for the $n\ell j$ core level from atom Q, with n the principal quantum no., ℓ the orbital angular momentum quantum no., and $j = \ell \pm 1$ the additional quantum no. if spin-orbit splitting is present, $E_{initial}(N)$ is the total initial state energy for the assumed N-electron system, and $E_{final}(N-1,Qn\ell\ j\ hole,K)$ is the Kth final-state energy for the (N-1)-electron system with a hole in the $Qn\ell j$ orbital. As an example, the six electrons in the *Mn 2p* subshell are split into *Mn* $2p_{1/2}$ (two electrons with m_j = *-1/2,+1/2*) and *Mn* $2p_{3/2}$ (four electrons with m_j = *-3/2,-1/2,+1/2,+3/2*). In general, there may be more than one final state associated with a given $Qn\ell j$ hole , with labels K = 1,2,…, as we discuss further below, e.g. in connection with multiplet splitting. Note also that, in the final state with the hole, all of the remaining electrons may relax slightly so as to try to screen the hole, thus lowering the total final energy by some amount that is often called the relaxation energy [3,4]. This relaxation/screening phenomenon has many consequences for the detailed interpretation of spectra. In many-electron theory, these effects are included in what is termed the "self-energy" correction.

As a final important quantity, we can write the intensity for excitation from a given core level to the *Kth* final hole-state associated with this level in the low-energy dipole limit as:

$$\begin{aligned} I(K) &\propto \left| \hat{\varepsilon} \bullet \left\langle \Psi_{final}(N-1,Qn\ell\ j\ hole,K + photoelectron) \left| \sum_{i=1}^{N} \vec{r}_i \right| \Psi_{initial}(N) \right\rangle \right|^2 \\ &\propto \left| \left\langle \Psi_{final}(N-1,Qn\ell\ j\ hole,K) \,|\, \Psi_{Initial}(N-1,Qn\ell\ j\ hole) \right\rangle \right|^2 \left| \hat{\varepsilon} \bullet \left\langle \varphi_{photoe} \left| \vec{r} \right| \varphi_{Qn\ell j} \right\rangle \right|^2 \end{aligned} \ , \qquad (3)$$

in which $\hat{\varepsilon}$ is the polarization of the radiation, the notation for initial and final state wave functions is obvious, $\vec{r}$ is one of three forms of the dipole operator that can be used interchangeably [3], the first line is an N-electron matrix element which emphasizes the inherent many-electron character of photoemission, and the second line involves a common simplifying step via the Sudden Approximation [3,4]. In this Approximation, the intensity is thus a product of the square of a one-electron matrix element which takes an electron from $\varphi_{Qn\ell j}$ to the photoelectron final state φ_{photoe} and the square of a simple (N-1)-electron overlap term with no operator between the initial state wave function with a hole in the $Qn\ell j$ subshell but

no relaxation/screening and one of the actual final ionic states *K* which includes such relaxation/screening. The approximation is often made of considering only the last one-electron factor in Equation (3), but it should be kept in mind that various many-electron effects, or vibrational/phonon effects, or even rotational effects in molecules, can distribute intensity over several states *K* that go beyond the one-electron picture, as we discuss below.

Having thus considered a formal description of photoemission, we now illustrate in Figure 1 the various types of experiment possible. A photon of a given polarization, which may be linear, circular, or elliptical in character, is incident on the sample surface at some angle θ_{inc}. Photons may be created from either laboratory sources (lasers, UV lamps, x-ray tubes), or synchrotron radiation. The photon is absorbed, exciting a photoelectron into the vacuum with some momentum $\vec{p} = \hbar\vec{K}$, where $\hbar = h / 2\pi$, $\vec{K}$ is the electron wave vector, and $\vec{s}$ is the electron spin, and finally into some kind of spectrometer for measuring kinetic energy. We here show the most commonly used spectrometer configuration, which consists of a set of concentric hemispherical deflection electrodes, although several other geometries are possible. In this hemispherical geometry, electrons of a given energy are focussed to a given radius (i.e. along a given *y* coordinate in the detection plane of Figure 1), such that integrating intensity over a given radius yields the first type of measurement: a photoelectron spectrum of number of electrons vs. kinetic energy or energy distribution curve (EDC), as shown schematically in Figure 1(a). An actual broad-scan or survey spectrum from a complex oxide sample of $La_{0.6}Sr_{0.4}MnO_3$ is shown in Figure 2, with various peaks labelled. Note here the presence also of Auger electron spectra, which are the result of non-radiative core-hole decay, and whose energies are somewhat more complicated to estimate, but in general involve three binding energies as follows:

$$E_{kinetic}^{Auger}(Z,123) \approx E_{binding,Z,1} - [E_{binding,Z,2} + E_{binding,Z+1,2}] / 2 - [E_{binding,Z,3} + E_{binding,Z+1,3}] / 2 \quad (4)$$

where the Auger kinetic energy results from an initial core hole in atomic level 1 of an atom with atomic number Z, which is filled by an electron from level 2 dropping into level 1, thus exciting an electron from level 3, or by an electron from level 3 dropping into level 1, thus exciting an electron from level 2, with these two processes being indistinguishable. Note that the most accurate prediction of these energies involves binding energies for both atom Z and the next higher in atomic number at Z+1, via what is often called the Equivalent Core Approximation [3,4].

If the photoelectron emission direction is varied relative to the crystal axes of a single-crystal sample, by scanning the angles θ and ϕ in Figure 1, additional effects are seen, due to the scattering of the outgoing electron wave from various atoms in the sample. If the emission is from a core level that is necessarily highly localized on one atomic site, a photoelectron diffraction pattern is observed [5]. An example of this for O 1s emission from NiO(001) is shown in Figure 1(b). Such patterns can be used to determine near-surface atomic structures. If the emission is from a valence level that is delocalized over many sites due to chemical bonding and electronic band formation, additional anisotropy in emission is found, and this can be measured, for example, by taking advantage of another property of the hemispherical electrostatic analyzer with a two-dimensional (2D) imaging detector. In this case, a

2D image can be directly related to the binding energy versus electron momentum or electron wave vector inside the crystal $\vec{k}$, which is then in many cases directly relatable to the band structure, or more precisely the quasi-particle excitation spectrum of the material. An example of this for emission from W(110) is shown in Figure 1(c).

Some other aspects of the measurement possibilities that exist are also shown in Figure 1. If an additional sensitivity to electron spin is somehow built into the detector (e.g. by taking advantage of spin-orbit scattering of high-energy electrons from a heavy-atom target in Mott scattering), it is possible to measure also the electron spin, providing additional information of particular relevance to magnetic materials. Another inset in Figure 1(d) shows such a measurement for the valence bands of iron, clearly indicating the difference in the electronic state distributions of spin-up and spin-down electrons for this ferromagnet [6].

Beyond this, as indicated in Figure 1(e), one can vary the photon energy, by going significantly above and significantly below the energy regime from ~20-1500 eV that has been used in most prior photoemission measurements. Also, Figure 1(f) indicates that we can expand upon the spectrometer in order to turn it into a microscope, thus yielding spectral images as a function of lateral position on the sample: the *x* and *y* coordinates in Figure 1. This type of measurement is reviewed in detail elsewhere [7,8], so we will not consider it beyond one later example here. There are also newer types of measurements involving time resolution (again Figure 1(f)), in which some perturbation of the sample is made, e.g. by gas reaction with a surface or by short-pulse light excitation, and the spectra are measured as a function of time. Depending on the particular process involved, these measurements can be fruitfully carried out on timescales varying from minutes (for chemical reactions) to seconds to femtoseconds (for laser pump-and-probe experiments) [8,9,10]. Finally, Figure 1(g) indicates that it is possible with special differential pumping outside the sample region to carry out photoemission studies at up to several torr of pressure [11].

Of key importance in any such photoemission experiment, however, is the depth of sensitivity in a solid sample, which is controlled primarily by the inelastic attenuation length Λ_e, for the photoelectrons, perhaps as modified by elastic electron scattering to yield an effective attenuation length [12,13]. If inelastic scattering is assumed to be isotropic in the material, the intensity from a certain emission depth z will decay as $I(z) = I_0 \exp[-z / \Lambda_e \sin\theta]$, and the mean escape depth below a surface will be given simply by $\Lambda_e \sin\theta$, as shown in Figure 3(a). Typical curves of Λ_e versus electron kinetic energy are shown for graphite and germanium in Figures 3(b) and (c), with calculations being made via the much-used and reasonably accurate TPP-2M formula [13]. One expects for any material a minimum of Λ_e for energies in the range of 20-50 eV that is only about 5-10 Å in magnitude, and a generally increasing trend away from this, in particular going approximately as $E_{kinetic}^{0.75}$ as energy goes into the multi-keV range. The general shape of this curve is thus in a sense "universal", applying at least qualitatively to all elements and compounds, but in reality it is "non-universal" in that the actual values can be quite different from one substance to another, as is clear from Figures 3(b) and (c). The detailed behaviour at very low energies is also expected to be different for different materials, a topic of current discussion in connection with photoemission experiments with excitation energies of only 5-10 eV that are aimed at being more bulk sensitive. Historically, photon sources were first divided into two regimes, ultraviolet lamps in the ca.

20-40 eV range, leading to the term ultraviolet photoelectron spectroscopy (UPS), and x-ray tubes in the ca. 1-2 keV range, leading to the term x-ray photoelectron spectroscopy (XPS). Figure 3 thus makes it clear that one expects very different degrees of surface sensitivity in these two regimes, with typical Λ_e values of ~ 5-10 Å for UPS and ~ 20-30 Å for XPS. Synchrotron radiation now permits spanning this full range continuously, and in the last few years, has also permitted using photon energies up to 10-15 keV, which yield via the extrapolation above to Λ_e values of 50-200 Å; such measurements are thus appealing for the future as being more bulk sensitive, and represent another emerging area in photoemission to which we will return later [14].

2 Core-Level Photoemission

2.1 Intensities and the Three-Step Model

Because core levels are highly localized on a given atom, they provide various element-specific types of information concerning each atomic species present in a sample. We consider first the intensities of a given photoelectron peak, which will be proportional to the number of atoms of a given type, as weighted by their excitation probabilities. Figure 2 makes it clear that each atom may have several core-level signatures of its presence, including both photoelectron and Auger peaks.

A much-used approach for calculating and using photoelectron intensities from both core and valence levels is the so-called three-step model [3,4] which divides the process into three steps of: (1) penetration of the exciting photon beam into the surface, with some resulting intensity profile $I_{h\nu}(x,y,z)$, and the coordinates defined in Figure 1; (2) excitation of photoelectrons from each atom in the sample that are located at various depths *z*, which will be proportional to the differential photoelectric cross section of the particular level $n\ell j$ of atom *Q* involved (e.g. *Mn* $2p_{1/2}$ and *Mn* $2p_{3/2}$ in Figure 2), written as $d\sigma_{Qn\ell j}(h\nu)/d\Omega$ and dependent on photon energy and the experimental geometry; and (3) transport from depth z to the surface, which involves inelastic attenuation via Λ_e, as well as elastic scattering/diffraction and refraction at the surface barrier, with the latter controlled by the surface inner potential V_0 having typical values of 5-15 eV. The differential subshell cross section can most simply be calculated by using only the last one-electron factor in Equation (3), averaging over the possible final states reached from each Q$n\ell j$, and summing over the Q$n\ell j$ initial states (e.g. two for *Mn* $2p_{1/2}$ and four for *Mn* $2p_{3/2}$). In general, $d\sigma_{Qn\ell j}(h\nu)/d\Omega$ is a maximum near threshold, when the photon energy is equal to $E_{binding}^{Vacuum}(Qn\ell j)$, and steadily decreases as the energy increases, although it may not reach a maximum until some distance above threshold, and it may also exhibit local minima called Cooper minima for energies not too far above threshold [3,15]. Neglecting elastic scattering and surface refraction for simplicity, one can finally calculate a core-level intensity from:

$$I(Qnlj) = C \int_0^\infty I_{h\nu}(x,y,z)\rho_Q(x,y,z)\frac{d\sigma_{Qn\ell j}(h\nu)}{d\Omega} exp\left[-\frac{z}{\Lambda_e \sin\theta}\right]\Omega(h\nu,x,y)dxdydz \ , \qquad (5)$$

where C is a constant characteristic of the experimental geometry, $\rho_Q(x,y,z)$ is the density of atomic type Q at position x,y,z, and $\Omega(h\nu, x, y)$ is the solid angle of acceptance of the spectrometer for a given photon energy (or equivalently electron kinetic energy) and position on the sample surface. In principal, $I_{h\nu}(x,y,z)$ can be calculated from a knowledge of the source beam spot profile, the incidence angle, and the x-ray indices of refraction of the substances in the sample [16]; $d\sigma_{Qn\ell j}(h\nu)/d\Omega$ is known from atomic theory, and its evaluation requires knowing the polarization of the exciting radiation (cf. Equation (3)) [15,17,18], Λ_e can either be taken from experimental data [19] or estimated from semi-empirical formulas, as e.g. the much-used TPP-2M formula [13]; and $\Omega(h\nu, x, y)$, which is equivalent once integrated over x and y to the spectrometer intensity response function, can be detemined from reference-sample calibration measurements [20], Thus, it is in principle possible to measure $I(Qnlj)$ and determine the only remaining unknown $\rho_Q(z)$, which amounts to a quantitative chemical analysis of the sample. More detailed discussions of cross-sections and their angular dependence, as well as integrations of Equation (5) to yield closed-form formulas for various sample configurations (homogeneous semi-infinite sample, single overlayer on a semi-infinite sample, thin overlayer on a semi-infinite sample) are given elsewhere [3]. These form the basic core of quantitative surface analysis by XPS, but with recent reviews pointing out additional considerations in achieving the most accurate results, as e.g. elastic scattering and electron refraction in crossing the inner potential surface barrier V_0 [12, 13, 21, 22]. User-friendly computer programs in fact exist that include some of these complicating factors, and permit predicting spectra with reasonable accuracy [23].

A final important effect related to photoelectron intensities is *resonant photoemission (RPE)*, in which the photon energy is tuned so as to lie on a strong core-level absorption resonance (e.g. *Mn* $2p_{3/2}$ or L_3), with this providing a second interfering channel for photoelectron excitation in another level in the same atom (e.g. *Mn 3d*) [24]. The intensity of the second level can thus be dramatically increased or decreased, depending on the relative amplitudes and phases of the interfering channels. This effect can be very useful in enhancing the contributions of a given type of valence character to bonding (e.g. by enhancing the *Mn 3d* contributions to the valence spectra of a compound such as that shown in Fig. 2 [24]). It has also been pointed out that resonant photoemission can occur between levels on different atoms, as e.g. between *O 1s* and *Mn 3d* in the compound MnO [25], with this type of *multi-atom resonant photoemission (MARPE)* effect providing the potential of uniquely identifying near-neighbors to a given atomic species.

2.2 Varying Surface and Bulk Sensitivity

From Figure 3, it is clear that the degree of surface sensitivity can be enhanced/deenhanced systematically in two ways: by going to more grazing/more nearly normal emission angles θ, respectively, often referred to as angle-resolved XPS (ARXPS); or by altering photon energies so as to scan the photoelectron kinetic energy relative to the minimum in Λ_e. Both of these methods are being used successfully to better try to deconvolute the surface and bulk contributions that will always be present in photoemission spectra [22]. We will also later consider a third method, which makes use of x-ray standing waves to selectively probe at specific depths below a surface [26].

2.3 Chemical Shifts

Although core levels are still often thought of as not being affected at all by chemical bonding, and in fact, their orbitals do not mix in a quantum-mechanical sense into the valence bands or molecular orbitals responsible for bonding, core-level binding energies are extremely sensitive to the changes in valence-level charge distributions that take place as bonds form, as first pointed out by Siegbahn et al. [2]. Roughly speaking, if an atom is placed in an environment in which it effectively loses charge to more electronegative neighbors, its core electrons will experience an increase in the net coulombic attraction (which is always due to the sum of nuclear attraction and other-electron repulsion), and their binding energies will go up. Conversely, if an atom becomes more negatively charged in forming bonds to its neighbors, its core electrons will have lower binding energies. For an isolated atom and considering a core level that spatially overlaps very little with the valence level involved (that is, of different principal quantum no. *n*), the removal/addition of a valence electron will to first approximation result in a binding energy shift given by the following Coulomb integral [27]:

$$\Delta E_{Binding} \approx \pm K_{Core,Val} = \pm \int \varphi^*_{Core}(\vec{r}_1)\varphi^*_{Val}(\vec{r}_2)\frac{e^2}{|\vec{r}_1 - \vec{r}_2|}\varphi_{Core}(\vec{r}_1)\varphi_{Val}(\vec{r}_2)dV_1 dV_2 \,. \quad (6)$$

However, this is an overestimate in any real situation, as the bonding charge is not removed or added from infinity, but simply relocated to/from near-neighbor atoms [27]. Final-state effects in which the other electrons relax around a given core hole to screen it can complicate this picture, and the most accurate way to determine core binding energies in different environments and to analyze such "chemical shift" data is to calculate total all-electron energies with and without a given core hole present, as shown in Equation (2). But whatever the method of interpretation, the use of core-electron chemical shifts represents a very powerful way of detecting different chemical species in a complex system, with many examples of this in the literature, and several detailed tabulations of chemical shifts for many elements [28].

As an illustrative example of chemical shifts, we show in Figures 4(a)-(e) spectra from the very narrow *W 4f*$_{7/2}$ level of a W(110) surface that is initially very clean but has been exposed to molecular oxygen at 3 x 10^{-9} torr over a sequence of time-resolved measurements [9]. The high resolution of this low-energy synchrotron radiation experiment, combined with careful peak fitting of many spectra through the time sequence, permits resolving six different chemical/structural states of W: those at the clean surface, those in the "bulk" = layers below the surface, two structurally inequivalent types bonded to one adsorbed oxygen atom (O1a and O1b), and those bonded to two or three oxygen atoms (O2 or O3, respectively), with the different atomic geometries for five of these shown in Figure 4(f). These data thus illustrate the high sensitivity of core levels to chemical state and bonding position relative to the surface. We return to discuss the time dependence in these spectra in the last section of this paper.

As a second example of the use of such chemical shifts, in Figure 5(b), we show the temperature dependence of O 1s spectra from a complex metal oxide with formula $La_{0.7}Sr_{0.3}MnO_3$ which exhibits an effect called colossal magnetoresistance [29]. The oxide surface was here prepared by cleaving, or more precisely, fracturing, a single crystal in UHV, in order to avoid surface contamination. Firstly, these O1s spectra exhibit a main peak and a low-energy peak about 1.5 eV away. From various measurements, including varying the elec-

tron takeoff angle to change the degree of surface sensitivity (cf. Figure 3(a)), it is concluded that the peak at higher binding energy is due to O atoms near/at the surface, with the other peak representing O atoms deeper within the material and denoted "Bulk" in the figure. Now considering the changes in these spectra as temperature is varied from well below to well above the temperature at which long-range magnetic order disappears (the Curie temperature, T_C) and then cooled to near the starting temperature again, we see a distinct shift in the bulk O 1s peak as T goes above T_C, and a concomitant shift, broadening and loss of intensity in the O 1s surface peak. Upon cooling again to below T_C, both features return to their previous states. The bulk peak shift has been interpreted as a transfer of electron charge to Mn from the six octahedral O atoms surrounding each Mn atom [29]. We return to discuss the left panel (a) of this figure involving Mn 3s emission in the next section.

2.4 Multiplet Splittings

Another very useful aspect of core photoelectron spectra arises if a given atom exists in a situation in which the valence levels are only partially occupied. In such a case, and with neglect of relativistic effects for simplicity of discussion here, the valence electrons can couple with one another such that there is a net spin *S* and a net orbital angular momentum *L* on a given site. In the simplest Russell-Saunders or L-S coupling picture, this yields a state before an electron is emitted of the form that can be described e.g. for the ground state of a $3d^5$ configuration with S = 5/2 and L = 0 as a ^6S state, where the superscript is the spin multiplicity 2S+1 and the main symbol denotes the net orbital angular momentum as S, P, D, for L = 0, 1, 2, etc. However, when an electron is emitted from a core level with a given one-electron spin *s*, corresponding to spin projections m_s = *-1/2 or +1/2*, and a given one-electron orbital angular momentum ℓ, the new (N-1)-electron system of core subshell-with-hole plus partially-filled valence electrons can couple to various final states S_f and L_f of different energies, thus yielding more than one binding energy for emission from a single $n\ell$ core level. This is termed a "multiplet splitting" of core-level binding energies [3,30], and it can be generalized to include spin-orbit splitting and to apply to partially filled s, p, d, and/or f subshells.

In figure 6(a), we illustrate the origin of a simple type of multiplet splitting, for emission from a *3s* subshell of a Mn transition metal atom. In this case, there is no orbital angular momentum in the core electron left behind, so we only need consider the coupling of the net spin on the Mn atom before 3s emission, S_{Mn} , which can be assumed to be carried by its valence 3d electrons, with the spin of the *3s* electron left behind. The two final state energies then correspond to total spin quantum nos. of $S_f = S_{Mn}+1/2$ *and* $S_{Mn}-1/2$, and these can be considered to arise primarily from a coupling of the remaining Mn *3s* spin parallel to, or anti-parallel to, the net *3d* spin S_{Mn}, respectively. Because the energy-lowering exchange interaction only acts between electrons of parallel spin, and also requires non-zero overlap to be significant, the higher-spin state energy will be lowered through the following effective exchange integral between a *3s* orbital φ_{3s} and a valence-band (VB) *3d* orbital φ_{3d}:

$$J^{eff}_{3s,VB(3d)} \approx \int \varphi^*_{3s}(\vec{r}_1)\varphi^*_{3d}(\vec{r}_2)\frac{e^2}{|\vec{r}_1-\vec{r}_2|}\varphi_{3d}(\vec{r}_1)\varphi_{3s}(\vec{r}_2)dV_1dV_2\,, \qquad (7)$$

where *e* is the electron charge, and the energy splitting between the two states ΔE_{3S} can finally be estimated from the Van Vleck Theorem of atomic physics as:

$$\Delta E_{3s} \approx (2S_{Mn}+1)J^{eff}_{3s,VB(3d)}\,. \qquad (8)$$

Thus, we see that such splittings can be used to directly derive information on the spin of a magnetic atom, with other details also derivable from more complex multiplets involving $\ell > 0$ and spin-orbit coupling [31]. Figure 6(b) also shows an experimental spectrum from the compound MnF_2, which is highly ionic and involves an initial state of Mn $\ldots 3s^2 \ldots 3d^5\ {}^6S$, and final states of $\ldots 3s^1\uparrow \ldots 3d^5\ {}^7S$ and $\ldots 3s^1\downarrow \ldots 3d^5\ {}^5S$, with a large and easily measurable splitting of ΔE_{3s} = 5.8 eV [30, 32].

As a specific example of the use of such multiplets, Figure 5(a) shows the temperature dependence of the Mn 3s splitting in the colossal magnetoresistive oxide $La_{0.7}Sr_{0.3}MnO_3$, and it exhibits a distinct increase of about 1 eV or 20% over the same temperature range as the O 1s chemical shifts discussed previously. This increase has been interpreted as being caused by an increase in S_{Mn} that is equivalent to a net transfer of one electronic charge from the O atoms to Mn, an effect not observed previously [29].

2.5 Electron Relaxation, Screening and Satellite Structures

We have noted before that the presence of a core-electron hole, or indeed any electron hole, induces other-electron relaxation, screening or polarization around it. These effects are best described in a full many-electron theory, and they can lead in some cases to additional strong satellite features in spectra which again can provide information on the nature of the valence electronic structure.

One particularly dramatic example of this occurs in the *2p* spectra of certain 3d transition metals and their compounds. As an example, we show in Figure 7 the spin-orbit-split *Cu* $2p_{1/2}$ and $2p_{3/2}$ doublet spectral region for $CuCl_2$ [31]. In the simplest ionic picture, one would expect only two peaks here, but there are four, with each member of the doublet showing a very strong satellite at lower kinetic energy or higher binding energy. (Note the reversed energy scale from earlier spectra presented.) The explanation of these satellites lies in the fact that we can consider Cu in this compound to exist as $Cu^{2+}\ 3d^9$, with just one hole in the 3d subshell. In the final state with a 2p hole and no screening, we can have $Cu^{3+}\ \underline{2p_{1/2}}^1 2p_{3/2}{}^4 3d^9$ or $Cu^{3+}\ 2p_{1/2}{}^2 \underline{2p_{3/2}}^3 3d^9$, where we have underlined the subshell with a hole. Multiplet splitting can occur in these states, as indicated by the vertical bars from a theoretical calculation in the figure. However, screening can also occur in the final state via charge transfer from Cl to Cu, so as to form the closed shell $Cu^{2+}\ \underline{2p_{1/2}}^1 2p_{3/2}{}^4 3d^{10}$ or $Cu^{2+}\ 2p_{1/2}{}^2 \underline{2p_{3/2}}^3 3d^{10}$ and, since such transfer costs relatively little energy, such screening will lower the binding energy. In this closed-shell system, there is no multiplet splitting and the peaks are narrower. A key point here is that both final states (screened and unscreened) can be reached in photoemission, with their strengths depending upon how they are mixed in a final-state wave function that is in general a configuration-interaction mixture of both. That is, both types of final states are for the specific case of $2p_{3/2}$ emission to a first approximation a mixture of the form

$$\Psi_{final,i}(N-1) = C_{1,i}(2p_{1/2}^2 2p_{3/2}^3 3d^9) + C_{2,i}(2p_{1/2}^2 2p_{3/2}^3 3d^{10} + Cl\ hole) \quad , \qquad (9)$$

with i = 1,2. This implies, via the Sudden Approximation form of Equation (3), that, if the initial state is assumed to be pure $3d^9$, the intensity of the two mixed final states will be proportional to $|C_{1,i}|^2$ as the other overlap term will vanish due to the different symmetries of the functions involved. Although the actual wave functions can contain many more terms in

principal than we show here, this type of analysis in terms of final-state mixing coefficients is common in both multiplet and satellite theory, and is discussed in more detail elsewhere [3,31].

More examples of such combinations of satellite structures and multiplet splittings for other compounds and in connection with emission from other core levels, together with theoretical calculations, are shown elsewhere [30,31,32,33,34].

As another more complex example involving a metallic system, we show the 2p spectral region of ferromagnetic Ni in Figure 8(a), excited at 1100 eV photon energy and averaged over two different polarizations of the radiation (right circular = RCP and left circular = LCP) [35]. Since Ni, like Cu^{+2}, has roughly a configuration of $3d^9$ in its ground state, one sees for both polarizations a screened predominantly $3d^{10}$ peak and a predominantly $3d^9$ unscreened satellite in connection with each member of the doublet [35,36]. The more complex nature of the electronic structure of Ni even leads to some mixing of $3d^8$ into the higher binding energy regions of each member, as discussed elsewhere [36]. Experiment is compared in this figure with (b) one-electron theory [35] and (c) a more accurate many-electron theory [36], and it is obvious that the many-electron approach much better predicts the satellite structure.

2.6 Magnetic Circular Dichroism

In magnetic circular dichroism (MCD), the intensity of a photoelectron peak is somehow found to change when the polarization of the incoming radiation is changed from right circular (RCP) to left circular (LCP). MCD is thus defined as the difference of two intensities or I(RCP)-I(LCP), usually divided by the sum or the average of these two intensities to yield a fractional number. These effects were first observed and qualitatively interpreted in core-level photoemission from Fe [37], and these first experimental results are shown in Figures 9(a) and (b). A simple one-electron explanation of these results is illustrated in Figure 9(c) [37,38]. The spin-orbit interaction, represented here by a parameter λ, splits the six *2p* states into two $2p_{1/2}$ and four $2p_{3/2}$ states. Beyond this, one assumes a Zeeman-like splitting of the sublevels within each spin-orbit peak induced by an effective internal magnetic field of the ferromagnet and resulting from the exchange interaction; this is associated with a parameter ξ. These interaction parameters can be used in a one-electron Hamitonian, whose diagonalization yields the result that, in the main $2p_{3/2}$ peak, the sublevels m_j = *-3/2, -1/2, +1/2*, and *+3/2* are no longer degenerate, as shown in the figure. The same is true of the two $2p_{1/2}$ sublevels. These energy splittings are then combined with the different intensities expected for these levels through the appropriate atomic transition probabilities, which scale as third parameter Δ, and are represented by the heights of the vertical bars in the figure. The interchange of these intensities when the polarization is switched from RCP to LCP (or equivalently, the magnetization $\vec{M}$ is switched in direction as shown in the figure), then yields the expectation of an up-down character for the MCD profile across a given peak, as well as an opposite sign of the MCD for the $2p_{3/2}$ and $2p_{/2}$ peaks. This general form of MCD spectra has by now been observed in many 3d transition metal systems.

As a more recent example, we show in Figure 8 experimental MCD data for 2p emission from Ni [35], again together with one-electron [35] and many-electron [36] theoretical calculations. Although the MCD curves here are complex, they can be qualitatively under-

stood in terms of the same model. However, the situation in Ni is more complex due to the presence of the screening satellites discussed previously and the intermixing of various configurations in both the initial and final states. This complexity leads to additional structure in the MCD curves, which is not present in the one-electron theory [35], but is very well described by many-electron theory [36].

Because ferromagnetic order is necessary for MCD to be observed, measurements of this provide an element-specific measurement of magnetic order, and this technique has been used to study a variety of magnetic systems.

2.7 Photoelectron Diffraction and Holography

In photoelectron diffraction (PD), sometimes referred to as x-ray photoelectron diffraction (XPD) due to the higher excitation energies that are often used, a core-level photoelectron scatters from the atoms neighboring the emission site, so as to produce angular anisotropy in the outgoing intensity [5]. Figure 10(a) shows the qualitative effects expected for the simple case of emission from the bottom red atom and elastic scattering from the top blue atom in a diatomic molecule, and Figure 10(b) shows a quantitative calculation for emission from the C 1s subshell in an isolated CO molecule at 500 eV kinetic energy. Electron-atom elastic scattering is typically peaked in the forward direction, with this effect becoming stronger (that is, having a stronger and narrower forward peak) as energy increases [5]. For the CO case in Figure 10(b), the intensity in the forward direction is in fact enhanced relative to that expected without scattering (I_0 in the figure) by about three times. Thus, one expects in XPD curves both a forward scattering peak (sometimes referred to as forward focussing) along near-neighbor interatomic directions, as well as higher-order diffraction interference effects that one can also consider to be holographic fringes. Back scattering is weaker as energy increases, but Figure 10(b) shows that, even at 500 eV, there are still interference fringes in the backward direction, and such backscattering effects have in fact been used for adsorbate structure determination [39].

Such XPD effects can be modelled using the ingredients shown in Figure 10(c). The polarization $\hat{\varepsilon}$ of the light influences the directionality of the initial photoelectron wave (cf. Equation (3)), and, for emission from an s-subshell, the outgoing unscattered wave ϕ_0 has an amplitude proportional to $\hat{\varepsilon}\bullet\hat{k}$, where $\hat{k}$ is a unit vector in the direction of the photoelectron wave vector, and the photoelectron deBroglie wavelength will be given by $\lambda_e = h/|\vec{p}| = 2\pi/|\vec{k}|$. In convenient units, $\lambda_e(\text{in Angstroms}) = \sqrt{150.5/E_{kin}(\text{in eV})}$. Thus, a 150 eV electron has a wavelength of about 1 Å, and a 1500 eV electron of about 0.3 Å, and these numbers are comparable to atomic dimensions. The outgoing photoelectron will elastically scatter from neighboring atoms j to produce scatterered-wave components ϕ_j. This process is describable in first approximation by plane-wave scattering, or more accurately by spherical-wave scattering. This scattering can be incorporated into a scattering factor f_j, which is furthermore found to be strongly peaked in the forward direction for energies above about 500 eV, as noted previously. The photoelectron wave components will also be inelastically attenuated as they traverse some total pathlength L in getting to the surface, with their amplitudes decaying as $exp(-L/2\Lambda_e)$. Finally, they will be refracted at the inner potential barrier V_0. Summing up all wave components (unscattered and scattered) and squaring then yields the diffraction pattern.

Due to the combined effects of the 1/r decrease in amplitude of ϕ_0 in moving away from the emitter and the inelastic scattering of all components, only atoms within some cluster surrounding the emitter (the dashed envelope) need to be considered in this sum, with the number of scatterers required varying from 5 or so to a few hundred, depending on the emitter position in the cluster and the photoelectron energy. Electrons can also be multiply scattered from several atoms in sequence, and accurate calculations of the resulting photoelectron diffraction patterns require including this for many cases, especially if scatterers are somehow lined up between the emitter and the detection direction, as is the case along low-index directions in multilayer emission from a single crystal. Various programs are now available for calculating XPD patterns, with one web-based version being particularly accessible [40] and other programs also available [41].

As one example of a photoelectron diffraction pattern, we show in Figure 11(a) the full-hemisphere intensity distribution for Fe 2p emission at 778 eV ($\lambda_e = 0.44$ Å) from a monolayer of FeO grown on a Pt(111) surface [42]. At this energy, the forward-peaked nature of f_O is observed to create strong peaks in intensity along the Fe-O bond directions. The angle of these peaks can furthermore be used to estimate the distance between the Fe and O atoms in the overlayer, and it is found to be only about half that for similar bilayer planes in bulk FeO, as illustrated in the bottom of Figure 11(a). Figure 11(b) also illustrates the element-specific structural information available from XPD. The Pt 4f XPD pattern from the same sample is rich in structure due to the fact that emission arises from multiple depths into the crystal, with forward scattering producing peaks and other diffraction features along low-index directions. The Fe 2p pattern is here just a projection onto 2D of the 3D image in Figure 11(a). The O 1s pattern shows only very weak structure, as the O atoms are on top of the overlayer, with no forward scatterers above them, and only weaker back scattering contributing to the diffraction pattern. Comparing the Fe and O patterns thus immediately permits concluding that Fe is below O in the overlayer, rather than vice versa.

Other examples of photoelectron diffraction in the study of clean surfaces, adsorbates, and nanostructure growth appear elsewhere [5, 39, 43], including a discussion of an alternative method of PD measurement in which the geometry is held fixed and the photon energy is scanned [5, 44].

Finally, we note that a photoelectron diffraction pattern can to a first approximation be considered a hologram [45], as suggested by the notation of reference wave and object wave in Figure 10(a). This has led to a number of studies in which diffraction patterns at various angles and/or various energies have been mathematically transformed so as to directly yield atomic positions in space [46]. More precisely, if the photoelectron diffraction intensities I are measured over several angles and/or energies, equivalent to some volume in $\vec{k}$-space, and then normalized by subtracting out the smoother unscattered intensity profile I_0 corresponding to the reference wave (cf. Figure 10(b)) to yield a function $\chi(\vec{k}) = [I(\vec{k}) - I_0(\vec{k})] / I_0(\vec{k})$, then the holographic image of the atoms neighboring the emitter $U(\vec{r})$ can be obtained from

$$U(\vec{r}) = \left| \iiint \chi(\vec{k}) \exp[i\vec{k} \bullet \vec{r} - ikr] d^3k \right| , \qquad (10)$$

where the phase factor is that appropriate to the phase difference between the reference wave and an object wave scattered from point $\vec{r}$, and the integral is over the volume in $\vec{k}$-space covered by the data points.

In Figure 12, we show a holographic image obtained using Cu 3p photoelectron intensities above a Cu(001) surface, with the emitter (e) as the central reference point [47]. These images were actually obtained using a differential approach in which two holograms at slightly different energies are subtracted from one another so as to suppress forward scattering effects, which are deleterious as far as holography is concerned. Using this approach, it is clear that one can image about 15 near-neighbor atoms below and to the sides of the emitter. Other future possibilities with photoelectron holography are discussed elsewhere [46].

3. Valence-Level Photoemission

3.1 Band-Mapping in the Ultraviolet Photoemission Limit

At lower energies of excitation, especially below roughly 100 eV, photoemission spectra are routinely used to map the band structure of solids and surfaces, and this is one of the most powerful applications of photoelectron spectroscopy. This ability is due to the fact that the excitation can be considered to be dominated by so-called "direct transitions" in which an occupied initial one-electron Bloch-wave state $\varphi(E_i,\vec{k}_i)$ at energy E_i and wave vector $\vec{k}_i$ can in the dipole limit only make a transition to a final state with wave vector $\vec{k}_f = \vec{k}_i + \vec{g}$, where $\vec{g}$ is some reciprocal lattice vector associated with the crystal structure under investigation. The relevant vector quantities and conservation equations are illustrated in Figure 13. Determing $\vec{k}_f$ inside the surface from a measurement of $\vec{K}_f$ outside the surface and then the set of $\vec{g}$ vectors which project it back into the reduced Brillouin zone in which the band structure is usually described thus permits directly measuring $E_{binding}(\vec{k}_i) = E_i(\vec{k}_i)$, the band structure, or if final-state screening and many-electron excitations are taken into account, more properly the spectral function as calculated from some sort of many-electron theory [4]. The need to accurately define the direction of $\vec{K}_f$, and thus also $\vec{k}_f$ inside the surface, leads to such measurements often being termed angle-resolved photoemission or ARPES. If the final photoelectron state is high enough in energy, it can be approximated as a free-electron, with $E_f(\vec{k}_f) \approx p_f^2/2m_e = \hbar^2 k_f^2/2m_e$, where m_e is the electron mass. This is just the non-relativistic kinetic energy inside the surface, which is higher by V_0 than the kinetic energy outside of the surface (cf. Figures 10 and 13). In convenient units, $k_f(\text{Å}^{-1}) = 0.512[E_f(\text{eV})]^{1/2}$.

To link the direct-transition picture to fundamental matrix elements via Equation (3), we can simply convert $\left|\hat{\varepsilon}\bullet\left\langle\varphi_{photoe}\left|\vec{r}\right|\varphi_{n\ell j}\right\rangle\right|^2$ to a transition between Bloch functions, yielding in a one-electron picture

$$I(E_f,\vec{k}_f) \propto \left|\hat{\varepsilon}\bullet\left\langle\varphi_{photoe}(E_f = h\nu + E_i, \vec{k}_f = \vec{k}_i + \vec{g}\left|\vec{r}\right|\varphi(E_i,\vec{k}_i)\right\rangle\right|^2, \qquad (11)$$

with obvious notation and an explicit inclusion of energy and wave-vector conservation in the final state. Figure 13 also illustrates that, in travelling from the interior of a solid to the surface, inelastic attenuation can occur (just as in the three-step model of core emission). Two additional things occur in crossing the surface: the electron wave can be scattered from a surface reciprocal lattice vector $\vec{g}_{surf}$ that may be different from the bulk $\vec{g}$ vectors, and finally,

in traversing the surface potential barrier V_0, the electron is decelerated and refracted from direction $\vec{k}_f$ into a new direction $\vec{K}_f$, which is actually what is measured. Momentum conservation in this last step assures that the component of $\vec{k}$ parallel to the surface is conserved, and this is very useful in studying systems whose electronic structure can be considered to be approximately two-dimensional and in the surface plane (as for example, surface electronic states and the high-temperature superconductors).

Having thus introduced the basic physics of ARPES, we now consider a couple of illustrative examples, including looking ahead to what happens as the photon energy is gradually increased into the keV or even multi-keV regime. In Figure 14, we show some recent ARPES results obtained for W(110) with an excitation energy of 270 eV and a display-type detection system such as that shown in Figure 1(c) [48]. In (a), we show the one-electron energy bands for W, plotted along the Γ-to-N direction in the reduced Brillouin zone (BZ), whose high-symmetry points are shown in (b). In (c), we show as a color contour plot experimental data obtained over an emission angle range that corresponds closely to scanning the emission point roughly along Γ-to-N in the BZ, or more precisely along the violet curves shown in (b). Also overlaid in (c) are the allowed direct transitions expected using a simple free-electron model for the final state. The agreement as to the positions and profiles of most of the experimental features in (a) is excellent, and confirms for this case the usage of ARPES for mapping band structure. But the simple model does not attempt to calculate the actual matrix element in Equation (11), so there is no information in it concerning intensities. To address this, we show as a color contour plot in Figure 14(d) the results of a much more sophisticated theoretical calculation which treats the emission process in one-step, explicitly calculating matrix elements [48]. The calculations in (d) agree well with the experimental results in (c) as to which features should be most intense, indicating the importance of matrix element effects in interpreting ARPES data in the future.

As a final example of ARPES, we consider its application to ferromagnetic Ni [49]. The experimental results in Figures 15(a),(c),(d) and (e) were obtained in a similar scan of the polar angle above a Ni(111) surface, but with a much lower excitation energy of 21.21 eV that is in fact more typical of many ARPES measurements, and a focus on a smaller range of energies close to the Fermi level. In the room temperature data of Figure 15(a), which correspond to $T/T_C = 0.80$, one clearly sees two split bands going up to the Fermi level, with intensity in fact visible above that level due to thermal excitation of electrons, and division of the data by the Fermi function from statistical physics. This splitting corresponds to a direct measurement of the expected exchange splitting of spin-up and spin-down bands in nickel, and is in good agreement with the results of theoretical calculations shown in Figure 15(b), although theory predicts a splitting about 30% too large, probably due to a lack of adequately treating many-electron effects in the photoemission process. In panels (c)-(e) of Figure 15 are shown measurements for the same polar scan, but at three temperatures spanning from well below to significantly above T_C. Here one sees what is probably the closing of the exchange splitting as temperature increases to the point where long-range ferromagnetic order is lost, again a most fundamental observation in the electronic structure of a ferromagnet.

There are many other examples of ARPES being used to study the fundamental properties of electronic structure, including strongly correlated materials such as high T_C [50] and

colossal magnetoresistive oxides [51], surface states [52], and quantum well states in nanoscale layers [53]. A powerful aspect of many of these studies that we have not focussed on here is looking only at the electrons near the Fermi level, with these being key to transport in some of the cited examples. Such Fermi surface mapping is thus another significant aspect of current ARPES studies.

3.2 Densities of States in the X-Ray Photoemission Limit

As energy is increased in valence-level photoemission, several factors act to smear out the region in $\vec{k}$ -space that is sampled, finally leading to a measurement that in first approximation measures the total density of electronic states at a given binding energy, as summed over all $\vec{k}$ values:

- As the magnitude of $\vec{k}_f$ increases, the finite angular resolution of the electron spectrometer implies that the definition of points in the BZ is smeared out, as illustrated in Figure 16(a) for photoelectron excitation from W along the [010] direction with a typical XPS energy of 1254 eV, and in Figure 16(b) for excitation at 10,000 eV. With the moderately high angular resolution of ±1.5° shown in (a), it is clear via the shaded disc that the set of $\vec{k}_i$ values involved is significantly broadened with respect to the size of the BZ. However by now, 2D imaging spectrometers such as that shown in Figure 1(c) have increased the resolution to ~0.1°, so this may not be the most serious factor, at least for energies up to 1 keV or so. Nonetheless, Figure 16(b) makes it clear that angular resolution must be increased significantly if the excitation energy goes up into the 10-keV regime, for which an angular resolution of 0.5° yields about the same fractional broadening in the BZ as 1.5° does for 1.2 keV excitation.

- Also as the magnitude of $\vec{k}_f$ increases, the effects of phonon creation and annihilation in the photoemission process must be considered. As an alternate view of this, the direct transitions in photoemission can be considered heuristically as a type of Bragg reflection, with $\vec{g} = \vec{k}_f - \vec{k}_i$ providing the additional momentum to the photoelectron. Thus, by analogy with normal diffraction in crystals, one might expect to suppress the intensity in the DT features due to atomic vibrations that reduce the degree of translation symmetry of the crystal according to a Debye-Waller factor, which can be written as: $W(T) \approx exp[-g^2 \langle u^2(T) \rangle]$, with $\langle u^2(T) \rangle$ the mean-squared vibrational displacement at temperature T. This factor effectively allows for the transfer of momentum to phonons, further smearing the specification of $\vec{k}_i$ in the BZ (cf. Figure 13). Qualitatively, one expects the Debye-Waller factor to represent the fraction of intensity in DT features that is not influenced by phonons. Calculations of this for various elements indicate that such effects often will give rise to essentially full BZ averaging at excitation energies in the 1-2 keV regime that are typical of classical XPS measurements [54].

- A final effect at higher excitation energies has to do not with smearing of the $\vec{k}_i$ definition in the BZ, but with a shift of position due to the photon momentum or wave vector, as given by $k_{h\nu} = 2\pi\nu / c$. In convenient units, this is $k_{h\nu}(\text{in Angstroms}^{-1}) = 0.000507(\text{Photon energy in eV})$. The need to consider this in fact involves a breakdown of the dipole approximation for the interaction of the radiation with the system. Thus, the overall wave-vector conservation equation is as given in Figures 13 or 16(a), with the magnitude of $\vec{k}_{h\nu}$ being explicitly shown for excitation at both 1254 eV and

10,000 eV. It is clear that such effects need to be allowed for at such high excitation energies, as first pointed out some time ago [54]. However, they are usually neglected at energies less than about 100 eV, for which $k_{h\nu} < 0.05$ Å^{-1}.

Taking the first two of these effects into account, one expects higher-energy valence spectra to reflect the total density of states of the material, modulated by whatever matrix elements are appropriate to the different types of states involved, as e.g. *nd* vs. *(n+1)s* and *(n+1)p* states in transition metals, with $n = 3$, 4, or 5. This is often termed the "XPS limit".

To illustrate this XPS limit, we show in Figures 17(a) and (c) the valence spectra for Au [55] and Ag [56] excited by 1.5 keV photons, as compared to broadened theoretical densities of states. For these metals at room temperature, the Debye-Waller factors with this excitation energy are very small, at about 0.04, so one expects rather full BZ averaging, especially in view of the rather large angular acceptances of the spectrometers involved. That this is indeed the case is evident from the very good agreement between the spectra and the broadened densities of states. Figure 17(b) further shows what occurs when the photon energy is increased to 5.5 keV [57], for which the energy resolution is in fact better than for the 1.5 keV data, at about 80 meV; the Debye-Waller factor is only about 6 x 10^{-6}; and the fine structure is again found to agree rather well with a suitably broadened density of states from local-density (LDA) theory [58]. Note, however, that it is necessary to shift the theoretical density of states by about 0.6 eV to higher binding energy to best match the position of the dominant 5d-band density of states features. This kind of discrepancy is well known in such comparisons of experiment with LDA theory, and is due to the fact that the different states in Au (more localized Au 5d vs more delocalized and free-electron-like Au 6s,6p) exhibit different screening/self-energy corrections due to many-electron interactions. Also, comparing Figures 17(a) and (b), we note the same sorts of minor discrepancies between theory and experiment in the dominant Au 5d region, which may have to do with matrix-element effects that are not included when simply comparing experiment to the density of states.

Thus, even though there is inherently more information content in an ARPES spectrum for which BZ selectivity is involved, spectra in the XPS limit still provide important clues as to the electronic structure of any material, and if they are measured at higher excitation energies, they also more closely express bulk, rather than surface, electronic properties.

As a last topic in this section, we consider an intermediate case for which both BZ selectivity and phonon smearing are involved. We show in Figures 18(a)-(d) a set of angle-resolved data from W(110) obtained with an intermediate energy of 870 eV, and at four different temperatures, which permits assessing the influence of phonons in a more quantitative way [48]. The four experimental panels clearly show band-mapping features, and in fact are also along the Γ-to-N direction sampled at lower energy in Figure 14, but running in the opposite direction. Note the similar positions and shapes of features between the two figures. However, it is also clear that raising the temperature stepwise from 300 K to 780 K, or from 0.75 times the Debye temperature that is characteristic of the W phonon spectrum to 1.95 times that temperature involves a smearing of those features and a significant gain of intensity in other parts of the angle-resolved data. In Figure 18(e) we show energy distribution curves (EDCs) at different temperatures as derived by integrating intensity over a small band in $\vec{K}_f$

for emission from near a high-symmetry point in the BZ, and in Figure 18(f) momentum distribution curves (MDCs) derived by integrating over a small band in energy at about 2 eV binding energy. A broadened density of states is also shown in (e) for comparison. Not surprisingly both EDCs and MDCs show a loss of fine structure as temperature is raised, with the highest temperature data beginning to converge to the W density of states, but clearly not reaching it, especially for the MDCs, which would be flat lines in this limit. Thus, the DOS limit is not quite reached by 780K for this case, consistent at least qualitatively with the Debye-Waller factor of 0.41; that is, roughly 40% of the intensity is still estimated to be via direct transitions.

Looking ahead, we note that the results of Fig. 18 suggest it should be possible to carry out more bulk-sensitive electronic structure studies at higher photon energies than have been typically employed in the past. However, a note of caution is in order, as W is one of the most cooperative materials in this respect [54], and it will in general require some combination of high angular resolution, not-too-high photon energy, and cryogenic cooling to achieve this for other materials, as discussed recently [48].

4 Some New Directions

4.1 Photoemission with Hard X-Rays

Within the last few years, interest has arisen in carrying out core and valence photoemission with excitation energies significantly above those of up to about 2 keV used to date. Such measurements have been carried out in the 3-15 keV regime, and a small number of groups in Europe and Japan have succeeded in designing beamline-end station combinations that permit carrying out such experiments with acceptable intensity/resolution combinations [14].

The principal reason for this emerging interest lies in the extrapolation of curves such as those in Figure 3 to higher energies, which we have noted involves inelastic Λ_e values of 50-200 Å. Thus, photoemission becomes a much more bulklike probe, and one that can look more deeply into multilayer or complex nanostructures. Two international workshops have so far explored this topic and its future [14].

As one example of what has been termed hard x-ray photoelectron spectroscopy (HAXPES or HXPS), we show in Figure 19 some Si 1s spectra excited from a multilayer structure of 120 Å of NiGe on top of 120 Å of SiO_2 on top of a deep Si substrate by 7.9 keV photons [59]. The resulting kinetic energies of about 6.1 keV permit seeing both types of Si atoms, with the spectra showing a chemical shift associated with elemental Si in the substrate and oxidized Si in the overlayer. Furthermore, varying the takeoff angle from near normal to more grazing so as to enhance surface sensitivity is found to dramatically change the intensity ratio of element to oxide. These data thus illustrate the power of HXPS, or more particularly angle-resolved HXPS (ARHXPS), to look into multilayer device structures or other structures of relevance to technology or environmental science. Beyond being able to probe more deeply below the surface, ARHXPS has additional advantages as compared to standard ARXPS; in analyzing data, it is possible to much more nearly neglect effects due to elastic scattering (which is much more forward peaked), refraction due to the inner potential (which

becomes much smaller compared to the electron kinetic energy), and surface inelastic scattering (which becomes negligibly small) [60,61].

As another example of what has been seen in HXPS, we show in Figure 20 temperature-dependent *Mn 2p* spectra from the same type of colossal magnetoresistive oxide sample involved in Figure 5. Here, data in Figure 20(a) with an excitation energy of 1090 eV, corresponding to kinetic energies of ~450 eV, and an inelastic attenuation length of ~10 Å [13,62], are compared with data in 20(b) obtained at 7700 eV, corresponding to kinetic energies of ~7050 eV, and an inelastic attenuation length of ~85 Å [13,63]. Thus, the latter is a much truer sampling of bulk properties. Although the general shape of the doublet is the same at the two energies, there are two significant differences. First and most obvious in the hard x-ray spectrum is a small, but very sharp, satellite that appears below T_C (which is 370K for this material) on the low binding energy side of the $2p_{3/2}$ peak, but which is absent in the lower-energy more-surface-sensitive spectrum. There is also an indication of the same satellite, although less well resolved, on the $2p_{1/2}$ peak, as indicated by the arrow. This type of satellite has been observed in HXPS from other manganite samples, and it has been interpreted as a screening satellite associated with highly delocalized electrons [64,65], with the implication that it requires the extended volume of a more bulk-sensitive measurement to see it. This satellite is also observed to slowly disappear as temperature is raised, which implies a connection with either magnetic order or a lattice that is free of the kind of Jahn-Teller distortion above T_C that is thought to produce the effects seen in Figure 5 [29]. A second difference between the hard x-ray and soft x-ray spectra is that a chemical shift with soft x-ray excitation of both *Mn 2p* components to higher binding energy by about 0.7 eV on lowering the temperature to about 150K that has been linked to the O-to-Mn charge transfer [62] discussed in connection with Figure 5 is difficult to discern with hard x-ray excitation. This suggests that the effects seen in Figure 5 are more localized near the surface.

One factor that will however limit the energy resolution achievable with HXPS, particularly for lighter atoms and/or solids with lower Debye temperatures, is the recoil energy involved in conserving both energy and momentum during photoelectron emission [66]. The recoil energy will be given approximately by

$$E_{recoil} \approx \frac{\hbar^2 k_f^2}{2M} \approx 5.5 \times 10^{-4} \left[\frac{E_{kin}(eV)}{M(amu)} \right] \quad , \tag{12}$$

where M is the emitter mass. Recoil has been shown experimentally to contribute to energy shifts and broadenings in both core and valence level spectra [66]. As representative numbers at the extreme excitation energy of 10 keV, the recoil energy will be 6.0 eV for H, 0.5 eV for C, 0.1 eV for Ni, and 0.03 eV for Au.

A number of other papers on HXPS have by now appeared, and are presented in overview elsewhere [14], but even at this early stage, it seems clear that such experiments have the potential to answer some key questions concerning the structure and composition of multilayer nanostructures, as well as the true bulk electronic structure of complex materials. As applied to valence spectra, it is likely that most HXPS spectra at moderate or higher temperatures will reflect the density of states in the XPS limit, but with a spectrometer of high angular resolution (e.g. well below 0.1°), at lower excitation energies in the few-keV range and/or

with cryogenic cooling, as well as with adequate correction for photon momentum, it should be possible to do more bulk-sensitive band mapping for some materials [48], even if not at the ultrahigh energy and angular resolutions available with much lower photon energies.

4.2 Photoemission with Standing-Wave Excitation

We have noted previously two ways to vary the surface sensitivity in photoemission: changing the photon energy so as to move along curves of the type in Figure 3 and varying the takeoff angle, as indicated e.g. in Figure 19. Both of these involve electron escape processes, so one can also ask if it is not possible to somehow tailor the photon wave field so as to provide a complementary avenue for varying surface sensitivity. Creating an x-ray standing wave is one method for doing this, and it has been found possible via this approach to selectively look at buried layers and interfaces [26, 67], as well as element-resolved densities of states [68], in this way.

In Figure 21, we illustrate one approach for using soft x-ray (or in the future also hard x-ray) standing waves to carry out more precise depth-resolved photoemission from multilayer nanostructures [26]. This approach combines a standing wave created by first-order Bragg reflection from a multilayer mirror of period d_{ML} with a sample that is grown on top of the multilayer, including a base layer of wedge profile. It is a simple matter to show that the profile of the 1st-order standing wave-modulated intensity, as given by $I_{hv}(x,y,z) \propto |\vec{E}(x,y,z)|^2$, where $\vec{E}$ is the electric field vector, will have a sinusoisal form with a period equal to the repeat distance of the diffracting planes or d_{ML}. If the standing wave is created by a typically well-focussed synchrotron radiation beam, then its dimensions will be much smaller than a typical sample, as indicated in the figure. Since the standing wave only exists in the region where the beam hits the sample surface, and its phase is locked tightly to the multilayer mirror, scanning the sample in the photon beam along the x direction in Figure 21 effectively translates the standing wave along the vertical z direction through the sample. In the example shown, the standing wave would in particular scan through the Fe/Cr interface of interest, at some x positions being more sensitive to the Fe side and at some other positions being more sensitive to the Cr side. This standing wave/wedge approach has been termed the "swedge" method" [69].

Some results obtained with this method for the Fe/Cr interface are summarized in Figures 22-24. In Figure 22(a), the two basic types of measurement possible are indicated: (i) a scan of sample position along x with the incidence angle fixed at or near the Bragg angle, as discussed previously; and (ii) a scan of incidence angle through the Bragg angle at fixed x, or equivalently fixed Cr thickness, which can be referred to by the usual term "rocking curve". The results of both types of scans on the Cr3p/Fe3p ratio are presented in Figures 22(b),(c). The roughly sinusoidal oscillations in this ratio in Figure 22(b) clearly reflect the passage of the standing wave through the interface. Figure 22(c) shows the more complex forms that are characteristic of rocking curves, with dramatic changes in the ratio in this data also. Self-consistently analyzing these data with x-ray optical calculations of standing-wave photoemission [70] and only two variable parameters (the depth of onset of the change in the Fe composition and the width of a linear gradient as the interface changes from pure Fe to pure Cr) yields the excellent fits shown to both types of data, and the parameters given at the left of Figure 24(a). In Figure 23 are shown MCD data for both Fe 2p and Cr 2p emission, which

have also been measured as the sample is scanned in the beam, with the variation as x or Cr thickness is varied being represented by the curves in Figure 24(b). The relative signs of the MCD in Figure 23 can be directly compared to those in Figure 9(b), and also immediately imply that a small amount of Cr is oppositely magnetized compared to Fe, and that this must be induced by the ferromagnetic Fe layer, since Cr is normally antiferromagnetic. Further analyzing this data via x-ray optical calculations with only two parameters for Fe 2p and 3p MCD and two parameters for Cr 2p and 3p MCD yields the atom-specific magnetization profiles shown at right in Figure 24(a). Thus, in this first published example, the swedge method permitted non-destructively determining the concentration profile through an interface, as well as the atom-specific magnetization contributions through it.

In more recent work, the swedge approach has also been used successfully to determine layer-specific densities of states that can be linked to changes in magnetoresistance as a function of nanolayer thicknesses []. Several other possible applications of it have also been suggested [16,26,69], including going to harder x-ray excitation, for which reflectivities and thus standing wave strengths can be much higher.

4.3 Photoemission with Space and Time Resolution, and at Higher Pressures

As Figure 1(f) indicates, other dimensions of photoemission involve adding *spatial resolution in the lateral dimensions x and y*, with one method for achieving additional resolution in the *vertical z dimension* already being discussed in the last section. In other papers in the ALC07 Conference, e.g. by Bauer, Koshikawa, Pavlovska, Quitmann and Schneider, the use of various techniques to add such lateral dimensions has been discussed in detail, and various aspects of such "spectromicroscopy" methods are reviewed in detail elsewhere [7,8]. Thus, we will here only specifically consider one future direction involving focussing the radiation to a small spot so as to do what has been termed "nano-ARPES" [71].

In Figure 25(a), the basic idea of the experiment is presented [71]. A zone-plate lens is used to focus a soft x-ray synchrotron radiation beam down to a spot of the order of 100 nm. A spectrometer like that shown in Figure 1 is then used to measure spectra from various regions of the sample by raster-scanning the sample in front of the beam in x and y. Both core and valence level spectra can be accumulated in this way. Figure 25(b) shows a micrograph from a cleaved sample of highly-oriented pyrolytic graphite (HOPG) in which the intensity in valence-band spectra has been used as a contrast mechanism. Looking in more detail at the ARPES spectrum from a specific 300 nm region reveals the band structure of the HOPG in that region. It is furthermore observed that the contrast comes about due to a slight tilting of different polycrystalline domains, with the brighter (yellow) regions corresponding to the so-called π-band of graphite being oriented towards the detector. Thus, one can look forward to taking advantage of much of what was discussed above with lateral spatial resolutions that should eventually reach 20 nm or better. In addition, spectromicroscopes making use of sophisticated electron optical elements promise to permit photoemission measurements below 10 nm, and perhaps at a few nm [72], although probably not with the energy and angular resolution of the scheme in Figure 25.

Time resolution in photoemission, e.g. in pump-probe experiments, that is by now down into the sub-nanosecond regime, and promises to go down into the femtosecond regime, is

also considered in other presentations at the ALC07 Symposium and elsewhere [8,10,73]. In some cases, these measurements have even combined lateral resolution with time and spin resolution [73], thus adding another key dimension for magnetic studies. Carrying out such spectromicroscopy measurements with standing-wave excitation, as demonstrated for the first time in a couple of first experiments [74] would add the final *z* dimension, thus permitting what might be considered a "complete" photoemission experiment in the sense of all of the variables indicated in Figure 1. These are clearly most promising areas for future development.

As another aspect of time-resolved photoemission, but one that often involves much longer timescales, we consider the *monitoring of surface chemical reactions in realtime*. As an early example of this type of measurement, Figure 4(g) shows the time evolution of the different types of W atoms on a W(110) surface that has been exposed to an oxygen pressure of 3.0×10^{-9} torr at room temperature, with the spectra in Figures 4(a)-(e) being snapshots along the way [9]. As noted earlier, the inherent narrowness of the *W 4f* levels, combined with high experimental resolution, permits resolving in these spectra six distinct types of W atoms: those at the clean surface, those in the "bulk" = layers below the surface, two structurally inequivalent types bonded to one adsorbed oxygen atom, and those bonded to two or three oxygen atoms, with the different atomic geometries shown in Figure 4(f). Being able to measure the time evolution of each of these features as shown in Figure 4(g) has permitted analyzing the chemical kinetics of the process, which here takes place on the scale of minutes [9].

Work in other laboratories has extended this type of reaction kinetics study to faster timescales and more complex chemical reactions [75,76], as well as to higher effective ambient pressures [11,75], thus permitting studies of such systems as aqueous solutions [77] and catalytic reactions [78] and representing yet another exciting area for future studies with photoemission.

As one technologically relevant example of these types of time-resolved reaction studies, Figure 26(a) shows a high-resolution spectrum of an oxidized Si(001) surface, with clear resolution of at least five distinct chemical states from the element to that of SiO_2. Such spectra have been used in the same way as those in Figure 4 to study the kinetics of oxidation of Si at pressures of about 10^{-6} torr, with resolution in time of all of the oxidation states [79]. As a more recent development, Figure 26(b) shows a high-pressure XPS system in which the sample is separated from the exciting synchrotron radiation beam by a thin Al (or SiN) window and from the analysis section of the electron spectrometer by an electron lens with two stages of differential pumping [11]. This configuration permits having the sample region at up to 5-10 torr in pressure during measurements. In this way, surface reactions can be studied at pressures that in some cases are much closer to the actual conditions of industrial processes or systems of relevance to environmental science, thus bridging what has been called the "pressure gap" between ultrahigh vacuum surface science research and real-world reaction conditions, and leading to the term "ambient pressure XPS (APXPS) [77,80]. As an example of the use of such a system, Figure 26(c) shows several spectra from a very recent Si oxidation study at 450 C and 1 torr which is of direct relevance to the processing conditions used in the semiconductor industry [80]. Spectra here were recorded every 8 seconds, compared to every 15

seconds in Figure 4, but they are shown here only about every minute. The SiO_2 thickness range covered is 0 to 25 Å. More detailed analysis of this data as shown in Fig. 27 indicates a clear division of the reaction rates into an initial rapid regime and a much slower quasi-saturated regime, with a break point between them that occurs when the SiO_2 is about 5-15 Å thick. Current models for the reaction kinetics of this process do not describe this regime of thicknesses that is now crucially important in devices [80].

Looking ahead concerning ambient pressure XPS, we expect that much shorter time-scales in the millesecond range and significantly better energy resolutions than those in Fig. 26(c) should be possible with brighter radiation sources, higher throughput spectrometers, and more efficient multichannel detectors that are under development [81].

Concluding Remarks

The photoelectric effect has indeed come a long way since Einstein, and in its present form, photoelectron spectroscopy/photoemission represents an incredibly diverse range of measurements that can tell us which atoms are present and in what numbers, in what chemical and magnetic states the atoms exist, how the atoms are arranged in space with respect to one another, the detailed picture of how these atoms are bound to one another, and finally how all this varies in space and time, and with ambient gas pressure. It is also clear that present instrumentation developments, for example, of new spectrometers and detectors, as well as brighter photon sources providing also better time resolution, will lead to other exciting new directions and capabilities that even Einstein might not have dreamed of. Finally, but importantly, advances in many-electron theory that we have not discussed in detail here should allow us to interpret these multidimensional data sets in a much more quantitative way.

Acknowledgements

This work was supported by the Director, Office of Science, Office of Basic Energy Sciences, Materials Science and Engineering Division, U.S. Department of Energy under Contract No. DE-AC03-76SF00098, by the Alexander von Humboldt Foundation and Helmholtz Association through a Helmholtz-Humboldt Award for the author, and by the Jűlich Research Center. The author is very grateful to Claus Schneider of the Jűlich Research Center and Wilfried Wurth of the University of Hamburg for acting as hosts for this award. The author also thanks L. Plucinski, J. Minar, Y. Takata, E. Rotenberg, Z. Yin, and W.E. Pickett for providing results prior to publication, and to S. Nunes for proofreading this manuscript.

Figure Captions

Figure 1 Illustration of a typical experimental configuration for photoemission experiments, together with the various types of measurements possible, including (a) simple spectra or energy-distribution curves, (b) core-level photoelectron diffraction, (c) valence-band mapping or energy vs $\vec{k}$ plots, (d) spin-resolved spectra, (e) measurements with much higher or much lower photon energies than have been

typical in the past, (f) measurements with space and time resolution, and (g) measurements at high ambient sample pressures of several torr. (With acknowledgement to Y. Takata for part of this figure.)

Figure 2 (a) A broad survey spectrum from the colossal magnetoresistive oxide $La_{0.6}Sr_{0.4}MnO_3$ obtained with excitation at 1253.6 eV, together with (b) an inset obtained at 950 eV over the region of the highest lying core levels and the valence levels. The highlighted O 1s and Mn 3s spectra have been studied as a function of temperature (see Figure 5). From ref. 29.

Figure 3 (a) A schematic diagram indicating the mean depth of photoelectron escape if elastic scattering and inner potential effects are neglected, together with electron inelastic attenuation lengths for two representative elemental solids, (b) graphite and (c) germanium. From ref. 13.

Figure 4 (a)-(e) High-resolution W $4f_{7/2}$ spectra excited with 100 eV radiation from a W(110) surface that was initially atomically clean but was exposed over a period of time to oxygen gas at a pressure of 3×10^{-9} torr. Six distinct chemical or structural states of W can be identified by the observed binding energy shifts: clean-surface W atoms, two types of W bonded to one oxygen atom, one type of W bonded to two oxygen atoms, one type of W bonded to three O atoms, and "bulk" W atoms located inward from the surface layer. (f) Geometric identification of the different atomic sites involved. The red figure is the unit cell of an ordered (2x2) oxygen structure. (g) Time dependence of the intensities of the resolvable features in a set of these spectra. From ref. 9.

Figure 5 Temperature-dependence of the Mn 3s and O 1s spectra from a freshly fractured surface of $La_{0.7}Sr_{0.3}MnO_3$ (cf. Figure 2). The two photon energies indicated have been chosen so that the photoelectrons in both cases have very nearly the same kinetic energy and thus the same inelastic attenuation lengths and surface sensitivity. From ref. 29.

Figure 6 Qualitative explanation of the multiplet splittings seen in 3s emission from some transition metal compounds, here illustrated for a Mn-containing substance. The inset at lower right shows a spectrum from the highly ionic compound MnF_2, excited by 1486.7 eV radiation. From refs. 3 and 30.

Figure 7 A Cu 2p photoelectron spectrum from $CuCl_2$, excited with 1486.7 eV radiation and with the dominant electron configurations of the "screened" $3d^{10}$ and the "unscreened" $3d^9$ satellite peaks indicated. From ref. 31.

Figure 8 (a) Experimental intensity and magnetic circular dichroism (MCD) results for Ni 2p emission from an epitaxial Ni overlayer with photons of 1100 eV energy, are compared to the results of (b) one-electron theory based on a spin-polarized relativistic KKR method. From ref. 35. (c) Intensity and MCD results from a many-electron theory. From ref. 36.

Figure 9 (a) The first magnetic circular dichroism data in core-level photoemission, for Fe 2p emission excited at 800 eV from Fe(110). The total intensity summed over RCP

and LCP polarization is shown at the top, above the individual RCP and LCP spectra. From ref. 37. (b) The resultant MCD spectrum, here obtained as $[I_{RCP} - I_{LCP}]/[I_{RCP} + I_{LCP}]$. (c) An explanation of the MCD in terms of one-electron theory. Here, the parameter λ represents the spin-orbit interaction, the parameter ξ a Zeeman-like exchange splitting of the different m_j sublevels, and the parameter Δ intensity. From refs. 37 and 38.

Figure 10 Illustration of various aspects of photoelectron diffraction. (a) Simple diffraction features expected in emission from one atom in a diatomic system. (b) An accurately calculated diffraction pattern for C 1s emission from an isolated CO molecule at a kinetic energy of 500 eV. Note the strong forward scattering peak, and other interference peaks or fringes extending from near the forward scattering direction to the backward scattering direction. (c) The basic theoretical ingredients required to describe photoelectron diffraction. From ref. 5, with calculations via the EDAC program of ref. 40.

Figure 11 X-ray photoelectron diffraction at 1486.7 eV excitation from a monolayer of FeO grown on Pt(111). (a) A full-hemisphere pattern for Fe 2p emission is shown, above the atomic geometry finally determined for this overlayer. (b) Diffraction patterns simultaneously accumulated for emission from Pt 4f (kinetic energy 1414 eV), Fe 2p (778 eV), and O 1s (944 eV). From ref. 42.

Figure 12 Holographic image of the atoms neighboring a given reference Cu atom below a Cu(001) surface. The typical reference emitter atom is noted by "e", and the neighbouring atoms are indicated in the inset.. The data yielding this image consisted of Cu 3p spectra at 25 kinetic energies from 77 to 330 eV and over 65 directions, thus representing about 1600 data points in k-space. From ref. 47.

Figure 13 Illustration of the basic processes and conservation laws in angle-resolved photoemission from valence levels.

Figure 14 Angle-resolved photoemission from W(110) with a photon energy of 260 eV. (a) The theoretical energy bands of W, plotted along the Γ-to-N direction that is very close to that sampled in the experiment. (b) The Brillouin zone of W, with the violet curve indicating the points sampled by direct transitions for the particular experimental geometry and angle scan involved. (c) An energy-vs-angle plot, or equivalently energy-vs-$\vec{k}$ plot, with brighter contours representing higher intensity. Also shown are the positions allowed via direct-transition wave-vector conservation and assumed free-electron final states. (d) Analogous color plot of more accurate one-step model calculations of this data. From ref. 48.

Figure 15 Angle-resolved photoemission from ferromagnetic Ni(111) with a photon energy of 21.2 eV. (a) Experimental data at room temperature and thus below the Curie temperature: the splitting of the bands due to the exchange interaction is seen. (b) Theoretical layer-KKR calculation of the bands involved in (a). (c) The temperature dependence of the spin-split bands, in going from below to above the Curie temperature. From ref. 49.

Figure 16 Illustration of $\bar{k}$ conservation in valence photoemission from W at two different photon energies: (a) 1253.6 eV, a typical soft x-ray energy also available with laboratory sources, and (b) 10,000 eV, a hard x-ray energy that is of interest for the future. Adapted from ref. 54.

Figure 17 Valence photoelectron spectra from the noble metals Ag and Au in the XPS or density of states limit. In (a) and (b), Au spectra with 1.5 keV and 4.5 keV excitation are shown. In both cases, the experimental results are compared with theoretical densities of states based on local-density theory. In (c), the same comparison is made for 1.5 keV excitation of Ag. From refs.55, 56, 57, and 58.

Figure 18 Temperature-dependent angle-resolved photoemission data from W(110) at an excitation energy of 860 eV. (a)-(d) Energy-vs-angle (energy-vs-$\vec{k}$) plots at four temperatures, with phonon-induced smearing of features evident as T is raised. From left to right in each, the N to Γ line in the Brillouin zone is approximately sampled. (e) Energy distribution curves (EDCs) integrated over a narrow angle (or $\vec{k}_i$) range for all four temperatures, with the curve at highest temperature also compared to a suitably broadened W density of states. (f) Momentum distributions curves (MDCs) integrated over a narrow binding energy range near 2 eV for all four temperatures. (g) The approximate region in $\vec{k}_i$ sampled by this data. From ref. 48.

Figure 19 Application of hard x-ray photoemission to a multilayer nanolayer structure combining a Si semiconductor substrate, an insulating SiO_2 layer, and a magnetic NiGe overlayer. Si 1s spectra have been obtained with 7.9 keV photons, and a variation of electron takeoff angle. Chemically-shifted Si and oxidized Si peaks are easily resolvable, and their relative intensities change markedly as the degree of surface sensitivity is enhanced at lower takeoff angles (cf. Figure 3(a)). From ref. 59.

Figure 20 Temperature-dependence of Mn 2p spectra from a freshly fractured surface of $La_{0.7}Sr_{0.3}MnO_3$, of the type studied in Figure 5. (a) With soft x-ray excitation at 1090 eV, a chemical shift to lower binding energy is seen on going above the Curie temperature. (b) With hard x-ray excitation at 7.7 keV, this shift is not evident, and a sharp low-binding-energy satellite is observed for a temperature below T_C. From refs. 29, 62, and 63.

Figure 21 Schematic illustration of the simultaneous use of an x-ray standing wave created by reflection from a multilayer mirror plus a wedge-profile overlayer sample to selectively study buried interfaces and layers—the "swedge" method. In the example here, a strong standing wave (SW) is created by first-order Bragg reflection from a multilayer made of repeated B_4C/W bilayers, and a Cr wedge underneath an Fe overlayer permits scanning the SW through the Fe/Cr interface by scanning the sample along the x direction. The two relevant equations for predicting the period of the standing wave along the z direction are also given. From ref. 26.

Figure 22 (a) The two types of scans possible in the swedge method: (i) Scanning along x or wedge thickness with θ_{inc} fixed at the Bragg angle to yield a direct scan of the

standing wave through the layers above the wedge, and (ii) scanning the incidence angle over the Bragg angle with x (or Cr thickness) fixed to yield a rocking curve. (b), (c) Experimental and calculated Cr3p/Fe3p ratios for these two types of scans. The best-fit theory curves are for the parameters shown at the left of Figure 24(a). From ref. 26.

Figure 23 Experimental MCD data for Fe 2p and Cr 2p emission from the sample of Figure 21, at two positions of the standing wave: emphasizing the interface (position B) and deemphasizing the interface (position C). From ref. 26 .

Figure 24 (a) The concentration and atom-specific magnetization profiles through the Fe/Cr interface, as derived by fitting x-ray optical calculations of photoemission [70] to the data of Figures 22 and 23. (b) The variation of Fe 2p and 3p MCD, and Cr 2p and 3p MCD, as about two cycles of the standing wave are scanned through the interface. From ref. 26.

Figure 25 Some first experimental results for spatially-resolved angle-resolved photoemission. (a) The basic experimental geometry, with a zone-plate used to focus the radiation into a small spot. (b) An image obtained by scanning the sample in front of the spot in x and y, with contrast provided by the intensity of the valence-band spectra. (c) Angle-resolved photoemission results obtained from a 300 nm region indicated in (b). From ref. 71.

Figure 26 (a) High-resolution Si 2p spectrum from a Si(001) surface that has been oxidized at 600° C and an ambient pressure of 5 x 10^{-7} torr. From ref. 79. (b) A spectrometer configuration in which the sample region is isolated from the radiation source by a thin window and from the spectrometer by differential pumping so as to permit ambient pressures up to 5-10 torr. From ref. 11. (c) A series of Si 2p spectra taken at about 1 min intervals during the oxidation of Si(001) at 450° C and an ambient pressure of 1 torr. From ref. 80.

Figure 27 The time-dependent growth of the SiO_2 layer on Si(001) at 450° C and various pressures, as derived from the relative intensities of the Si^{+4} and Si^{0} peaks in spectra such as those in Fig. 26(c). From ref. 80.

References

[1] A. Einstein, *Ann. Phys.* **17** (1905) 132.

[2] Some of the first developments in x-ray photoelectron spectroscopy are presented in two books: K. Siegbahn et al., *Atomic, molecular and solid-state structure studied by means of electron spectroscopy* (Nova Acta Regiae Soc. Sci. Ups. 20.1-282, 1967); and *ESCA applied to free molecules*, North-Holland Amsterdam, The Netherlands, 1969).

[3] C. S. Fadley, "Basic Concepts of X-Ray Photoelectron Spectroscopy", chapter in *Electron Spectroscopy: Theory, Techniques, and Applications*, C. R. Brundle and A. D. Baker, Eds.

(Academic Press, London, 1978) Vol. II, Chap. 1; available also a reprint at: http://www.physics.ucdavis.edu/fadleygroup/.

[4] S. Hűfner, *Photoelectron Spectroscopy: Principles and Applications, 3rd Edition* (Springer, Berlin, 2003).

[5] C. S. Fadley, "Surface Structure Studies Using Photoelectron Diffraction and Auger Electron Diffraction", chapter in *Synchrotron Radiation Research: Advances in Surface and Interface Science*, R. Z. Bachrach, Ed. (Plenum Press, New York, 1992).

[6] H.-J. Kim, E. Vescovo, S. Heinze and S. Blügel, Surf. Sci. 478 (2001) 193.

[7] E. Bauer, C. Koziol, G. Lilienkamp and T. Schmidt, J. Electron Spectros. and Rel. Phen. **84** (1997) 201.

[8] G. Schönhense, H.J. Elmers, S.A. Nepijko, and C.M. Schneider, Adv. In Imaging and Electron Phys. **142** (2006) 160.

[9] R.X. Ynzunza, R. Denecke, F.J. Palomares, J. Morais, E.D. Tober, Z. Wang, F.J. Garcia de Abajo, J. Liesegang, Z. Hussain, M.A. Van Hove, C.S. Fadley, Surf. Sci. **459** (2000) 69.

[10] M. Pickel, A.B. Schmidt, M. Donath, and M. Weinelt, Surf. Sci. **600** (2006) 4176; F. Banfi, C. Giannetti, G. Ferrini, G. Galimberti, S. Pagliara, D. Fausti, and F. Parmigiani, Phys. Rev. Lett. **94** (2005) 037601.

[11] D.F. Ogletree, H. Bluhm, G. Lebedev, C.S. Fadley, Z, Hussain, M. Salmeron, Rev. Sci. Inst. **73** (2002) 3872.

[12] C.J. Powell, A. Jablonski, I.S. Tilinin, S. Tanuma, D. R. Penn, . Electron Spectros. and Rel. Phen. **98** (1999) 1.

[13] S. Tanuma, C. J. Powell, and D. R. Penn, Surf. Interface Anal. **36** (2004) 1.

[14] Special journal issue dedicated to photoemission with hard x-rays, Nucl. Inst. and Meth. A **547** (2005), edited by J. Zegenhagen and C. Kunz; program and abstracts of recent international workshop on hard x-ray photoemission, HAXPES06, Spring8, Japan, available at: http://haxpes2006.spring8.or.jp/program.html.

[15] S. M. Goldberg, C. S. Fadley, and S. Kono, J. Electron Spectrosc. and Relat. Phenom. **21** (1981) 285.

[16] C. S. Fadley, S.-H. Yang, B. S. Mun, J. Garcia de Abajo, "X-ray Optics, Standing Waves, and Interatomic Effects in Photoemission and X-ray Emission", chapter in the book *Solid-State Photoemission and Related Methods: Theory and Experiment*, W. Schattke and M.A. Van Hove, Editors, (Wiley-VCH Verlag, Berlin GmbH, 2003).

[17] J.-J. Yeh and I. Lindau, "Atomic Subshell Photoionization Cross Sections and Asymmetry Parameters: $1 < Z < 103$," At. Data Nucl. Data Tables **32** (1985) 1, also available in graphical form at: http://ulisse.elettra.trieste.it/services/elements/WebElements.html.

[18] P. H. Scofield, "Theoretical Photoionization Cross Sections from 1 to 1500 keV", Lawrence Livermore Laboratory Report UCRL-51326, also available at: http://www.physics.ucdavis.edu/fadleygroup/Scofield.CrossSections.UCRL51326.pdf.

[19] The NIST Electron Inelastic-Mean-Free-Path Database (http://www.nist.gov/srd/nist71.htm) and the NIST Electron Effective-Attenuation-Length Database (http://www.nist.gov/srd/nist82.htm), which are available at no charge.

[20] M.P. Seah, S.J. Spencer, J. Electron Spectrosc. and Rel. Phen. **151** (2006) 178.

[21] Powell C.J., Jablonski A., Tanuma S., et al. J. Electron Spectrosc. and Rel. Phen. **68** (1994) 605.

[22] C.S. Fadley, "Angle-Resolved X-Ray Photoelectron Spectroscopy", Prog. In Surf. Sci. **16** (1984) 275; S. Oswald, M. Zier, R. Reiche and K. Wetzig, Surf. Interface Anal. **38** (2006) 590; Summary of the 47th IUVSTA Workshop on Angle-Resolved XPS, Riviera Maya, Mexico, March, 2007, to appear in Surface and Interface Analysis.

[23] For example, the SESSA program by W. Smekal, W. S. M. Werner, and C. J. Powell, and described in Surf. And Interf. Anal. **37** (2005)1059, includes all of the effects mentioned here except surface refraction due to V_0 and can be used over a very broad range of photon energies. Further information on this is available at: http://www.nist.gov/srd/nist100.htm and http://www.iap.tuwien.ac.at/~werner/sessa.html. An alternative program emphasizing the exact shape of spectra as produced by inelastic scattering is QUASES™ by S. Tougaard, with information on this available at: http://www.quases.com/.

[24] R. Hashimoto, A. Chikamatsu, H. Kumigashira, M. Oshima, N. Nakagawa, T. Ohnishi, M. Lippmaa, H. Wadati, A. Fujimori, K. Ono, M. Kawasaki, H. Koinuma, J. Electron Spectrosc. and Rel. Phen. **144–147** (2005) 479.

[25] A.W. Kay, F.J. Garcia de Abajo, S.-H. Yang, E. Arenholz, B.S. Mun, N. Mannella, Z. Hussain, M.A. Van Hove, and C.S. Fadley, Phys. Rev. B **63**, (2001) 115119 and earlier references therein.

[26] S.-H. Yang, B.S. Mun, N. Mannella, S.-K. Kim, J.B. Kortright, J. Underwood, F. Salmassi, E. Arenholz, A. Young, Z. Hussain, M.A. Van Hove, and C.S. Fadley, J. Phys. Cond. Matt. **14** (2002)L406.

[27] C. S. Fadley, S. B. M. Hagstrom, M. P. Klein, and D. A. Shirley, J. Chem. Phys. **48**, (1968) 3779 .

[28] NIST X-ray Photoelectron Spectroscopy Database, available at http://srdata.nist.gov/xps/.

[29] N. Mannella, A. Rosenhahn, C. H. Booth, S. Marchesini, B. S. Mun, S.-H. Yang, K. Ibrahim, Y. Tomioka, and C. S. Fadley, Phys. Rev. Lett. **92** (2004) 166401.

[30] C. S. Fadley and D. A. Shirley, Phys. Rev. A **2** (1970) 1109**.**

[31] G. Van der Laan, C. Westra, C. Hass, and G.A. Sawatzky, Phys. Rev. B **23** (1981) 4369.

[32] S.P. Kowalczyk, L.Ley, F.R. McFeely, R.A. Pollak, and D.A. Shirley, Phys. Rev. Lett. **7** (1973) 4009.

[33] A.E. Bocquet, T. Mizokawa, T. Saitoh, H. Namatame, and A. Fujimori, Phys. Rev. B **46** (1992) 3771**.**

[34] R. Denecke, J. Morais, R.X. Ynzunza, G. Fecher, J.G. Menchero, J. Liesegang, J.B. Kortright, Z. Hussain, and C.S. Fadley, Phys. Rev. B 65, (2002) 245421.

[35] G. Van der Laan, S.S. Dhesi, E. Dudzik, J. Minar, and H. Ebert, J. Phys. Condens. Matter **12** (2000) L275.

[36] J. Menchero, Phys. Rev. Lett. **76** (1996) 3208; Phys. Rev. B **57** (1998) 1001.

[37] L. Baumgarten, C.M. Schneider, H. Petersen, F. Schäfers, and J. Kirschner, Phys. Rev. Lett. **65**, (1990) 492.

[38] J.G. Menchero, Phys. Rev. B **57** (1998)993.

[39] T. Greber, J. Wider, E. Wetli, and J. Osterwalder, Phys. Rev. Lett. **81** (1998) 1654.

[40] Multiple scattering program *EDAC* for calculating photoelectron diffraction available at: http://csic.sw.ehu.es/jga/software/edac/index.html, with the methodology behind it described in F.J.Garcia de Abajo, M.A. Van Hove, and C.S. Fadley, Phys. Rev. B **63** (2001) 075404.

[41] Another general program for photoelectron diffraction calculations *MSCD*, including geometry optimization, is available at: http://www.ap.cityu.edu.hk/personal-website/Van-Hove.htm#Interactive_software.

[42] Y.J. Kim, C.Westphal, R.X. Ynzunza, Z. Wang, H.C. Galloway, M. Salmeron, M.A. Van Hove, C.S. Fadley, Surf. Sci. **416** (1998) 68.

[43] J. Osterwalder, A. Tamai, W. Auwarter, M.P. Allan, and T. Greber, Chimia **60** (2006) A795, and earlier references therein.

[44] D.P. Woodruff, Surf. Sci. Repts. **62** (1): 1-38 JAN 1 2007

[45] A. Szöke, in Short Wavelength Coherent Radiation: Generation and Applications, AIP Conf. Proc. No. 147, edited by D.T. Attwood and J. Boker (AIP, New York, 1986), p. 361.

[46] C.S. Fadley, M.A. Van Hove, A. Kaduwela, S. Omori, L. Zhao, and S. Marchesini, J. Phys. Cond. Mat. **13** (2001) 10517, and earlier references therein.

[47] S. Omori, Y. Nihei, E. Rotenberg, J.D. Denlinger, S. Marchesini, S.D. Kevan, B.P. Tonner, M.A. Van Hove, and C.S. Fadley, Phys. Rev. Lett. **88** (2002) 5504.

[48] L. Plucinski, J. Minar, B.C. Sell, J. Braun, H. Ebert, C.M. Schneider, and C.S. Fadley, to be published.

[49] T.J. Kreutz, T. Greber, P. Aebi, and J. Osterwalder, Phys. Rev. B **58** (1998) 1300.

[50] A. Damascelli, Z. Hussain, Z.X. Shen, Reviews of Modern Physics **75** (2003) 473-541.

[51] N. Mannella, W.L. Yang, X.J. Zhou X, H. Zheng, J.F. Mitchell, J. Zaanen, T.P. Devereaux, N. Nagaosa, Z. Hussain , and Z.X. Shen, Nature **438** (2005) 474.

[52] E.W. Plummer, Junren Shi, S.-J. Tang, Eli Rotenberg, S.D. Kevan, Prog. in Surf. Sci. **74** (2003) 251.

[53] E. Rotenberg, Y.Z. Wu, J.M. An, M.A. Van Hove, A. Canning, L.W. Wang, Z.Q. Qiu, Phys. Rev. B **73** (2006) 075426.

[54] Z. Hussain, C. S. Fadley, and S. Kono, Phys. Rev. B **22** 3750 (1980); R. C. White, C. S. Fadley, M. Sagurton, and Z. Hussain, Phys. Rev. B **34** (1986) 5226.

[55] K. Siegbahn, private communication.

[56] A. Barrie and N.E. Christensen, Phys. Rev B **14** (1976) 2442.

[57] Y. Takata, private communication.

[58] Z. Yin and W.E. Pickett, private communication.

[59] T. Hattori, H. Nohira, K. Azuma, K. W. Sakai, K. Nakajima, M. Suzuki, K. Kimura, Y. Sugita, E. Ikenaga, K. Kobayashi, Y. Takata, H. Kondo, S. Zaima, Int. J. High Speed Electronics **16** (2006) 353.

[60] C.S. Fadley, Nucl. Inst. and Meth. A **547** (2005) 24.

[61] L. Kover , M. Novak , S. Egri , I. Cserny , Z.Berenyi , J. Toth , D. Varga , W. Drube , F. Yubero , S. Tougaard , W.S.M. Werner , Surf. Int. Anal. **38** (2006) 569.

[62] N. Mannella, PhD thesis, University of California Davis, 2003; and N. Mannella, C. H. Booth, A. Rosenhahn, B. C. Sell, A. Nambu, S. Marchesini, B. S. Mun, S.-H. Yang, M. Watanabe, K. Ibrahim, E. Arenholz, A. Young, J. Guo, Y. Tomioka and C.S. Fadley, Physical Review B, submitted.

[63] F. Offi, N. Mannella, T. Pardini, G. Panaccione, A. Fondacaro, P. Torelli, S. Huotari, M. W. West, J. W. Mitchell and C.S. Fadley, Physical Review B, to appear.

[64] K. Horiba, M. Taguchi, A. Chainani, Y. Takata, E. Ikenaga, D. Miwa, Y. Nishino, K. Tamasaku, M. Awaji, A. Takeuchi, M. Yabashi, H. Namatame, M. Taniguchi, H. Kumigashira, M. Oshima, M. Lippmaa, M. Kawasaki, H. Koinuma, K. Kobayashi, T. Ishikawa, S. Shin, Phys. Rev. Lett. **93** (2004) 236401; H. Tanaka, Y. Takata, K. Horiba, M. Taguchi, A. Chainani, S. Shin, D. Miwa, K. Tamasaku, Y. Nishino, T. Ishikawa, E. Ikenaga, M. Awaji, A. Takeuchi, T. Kawai, K. Kobayashi, Phys. Rev. B **73** (2006) 094403.

[65] M. VanVeenendaal, Phys. Rev. B **74**, 085118 (2006).

[66] Y. Takata, Y. Kayanuma, M. Yabashi, K. Tamasaku, Y. Nishino, D. Miwa, Y. Harada, K. Horiba, S. Shin, S. Tanaka, E. Ikenaga, K. Kobayashi, Y. Senba, H. Ohashi, and T. Ishikawa, Phys. Rev. B **75** (2007) 233404; and Y. Takata et al., recoil measurements in HXPS valence spectra of aluminum, to be published.

[67] S.-H. Yang, B. S. Mun, N. Mannella, A. Nambu, B.C. Sell, S. B. Ritchey, F. Salmassi, S. S. P. Parkin, C. S. Fadley, J. Phys.: Condens. Matter **18** (2006) L259.

[68] J. Woicik, Nucl. Inst. and Meth. A **547** (2005) 227.

[69] S.-H. Yang, B.S. Mun, and C.S. Fadley, Synchrotron Radiation News **24** (2004) 17; and S.-H. Yang, B.C. Sell, and C. S. Fadley, Journal of Applied Physics, *in press*.

[70] S.-H. Yang, specially written computer program for standing-wave photoemission from multilayer structures, to be published.

[71] E. Rotenberg and A. Bostwick, private communication.

[72] T. Schmidt, U. Groh, R. Fink, E. Umbach, Surf. Rev. & Lett. **9** (2002) 223; H. Marchetto, U. Groh, T. Schmidt, R. Fink, H.J. Freund, E. Umbach, Chem. Phys. **178** (2006) 325.

[73] J.-P. Wustenberg_, M. Cinchetti, M. Sanchez Albaneda, M. Bauer, M. Aeschlimann J. Magn. and Magn. Mat. **316,** (2007) e411.

[74] J. Maul, J. Lin, A. Oelsner, D. Valdaitsev, N. Weber, M. Escher, M. Merkel, H. Seitz, U. Heinzmann, U. Kleineberg, G. Schonhense, Surf. Sci. **601** (2007) 4758; F. Kronast, A. Keiser, C. Wiemann, R. Ovsyannikov, A. Locatelli, D. Buergler, R. Schreiber, , S.-H. Yang, H. Dürr, C. Schneider, and C.S. Fadley, to be published.

[75] A.Baraldi, G.Comelli, S.Lizzit, M.Kiskinova, G.Paolucci, Surf. Sci. Repts. **49** (2003) 169.

[76] R. Denecke, Applied Physics A **80** (2005)977, and references therein.

[77] S. Ghosal, J.C. Hemminger, H. Bluhm, B.S. Mun, E.L.D. Hebenstreit, G. Ketteler, D.F. Ogletree, F.G. Requejo, and M. Salmeron, Science **307** (2005) 5709.

[78] H. Bluhm, M. Hävecker, A. Knop-Gericke, E. Kleimenov, and R. Schlögl, D. Teschner, V. I. Bukhtiyarov, D. F. Ogletree and M.B. Salmeron, J. Phys. Chem. B 108 (2004) 14340.

[79] Y. Enta, Y. Miyanishi, H. Irimachi, M. Niwano, M. Suemitsu, N. Miyamoto, E. Shigemasa, H. Kato, Phys. Rev B 57, 6294 (1998) and J. Vac. Sci. Tech. A **16** (1998) 1716.

[80] Y. Enta, B. S. Mun, Y. Enta, M. Rossi, P. N. Ross, Z. Hussain, C.S. Fadley, K.-S. Lee, and S.-K. Kim, Applied Physics Letters, to appear.

[81] J.-M. Bussat, C.S. Fadley, B.A. Ludewigt, G.J. Meddeler, A. Nambu, M. Press, H. Spieler, B. Turko, M. West, G.J. Zizka, IEEE Transactions on Nuclear Science **51**, (2004) 2341.

Some possible photoemission measurements

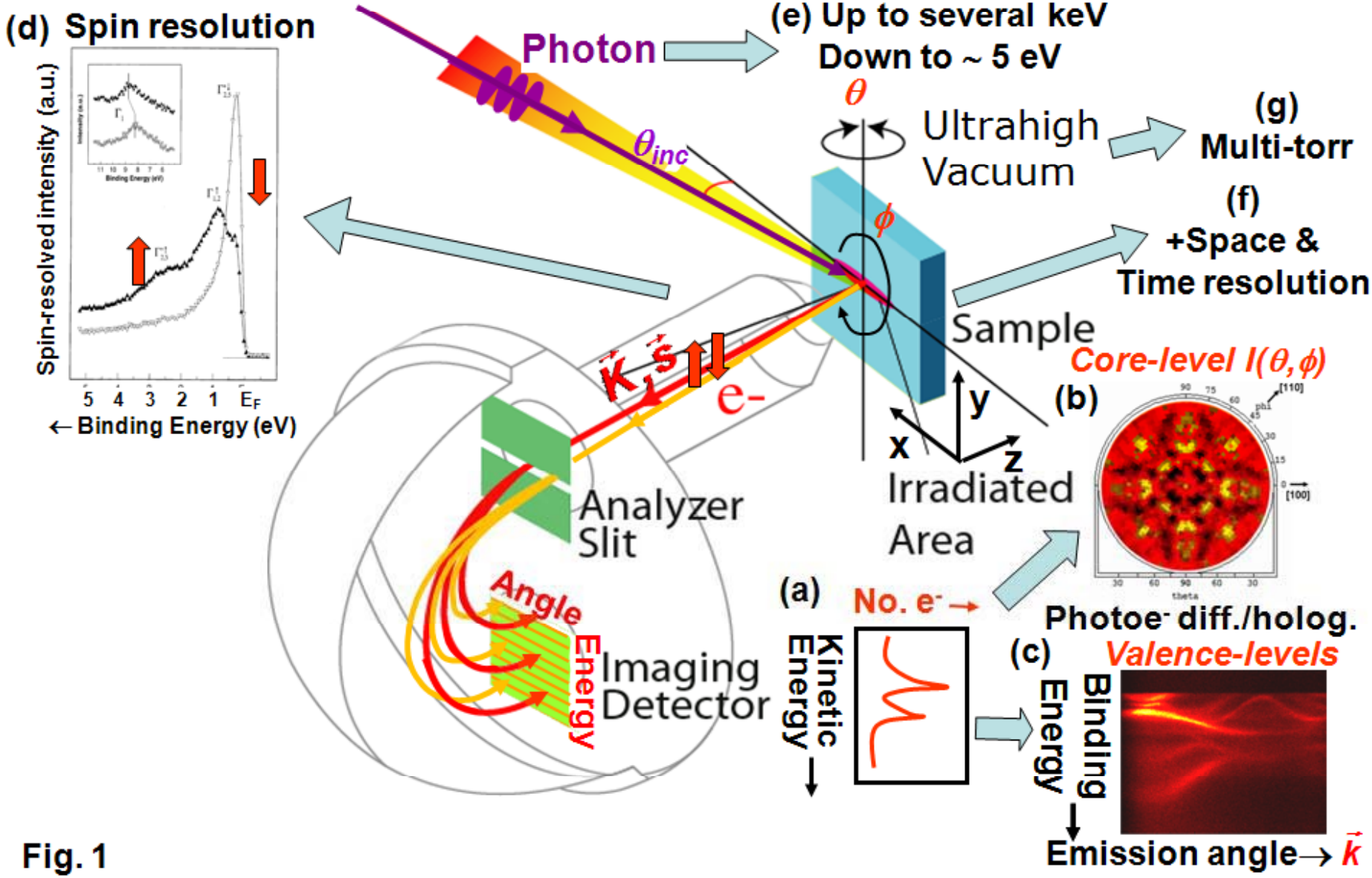

Fig. 1

Core and valence photoemission

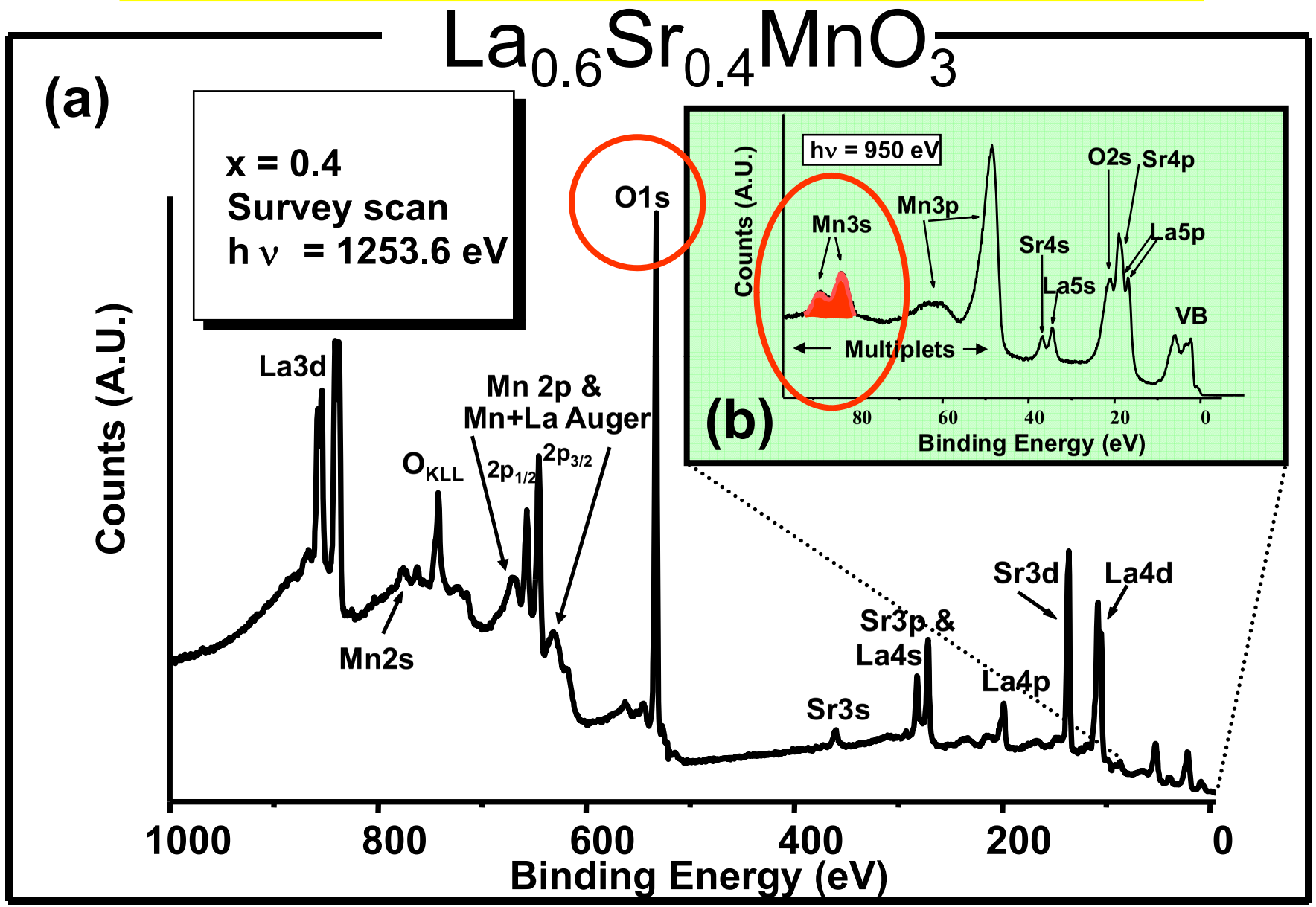

Fig. 2

Electron inelastic mean free paths in solids—the "non-universal curve"

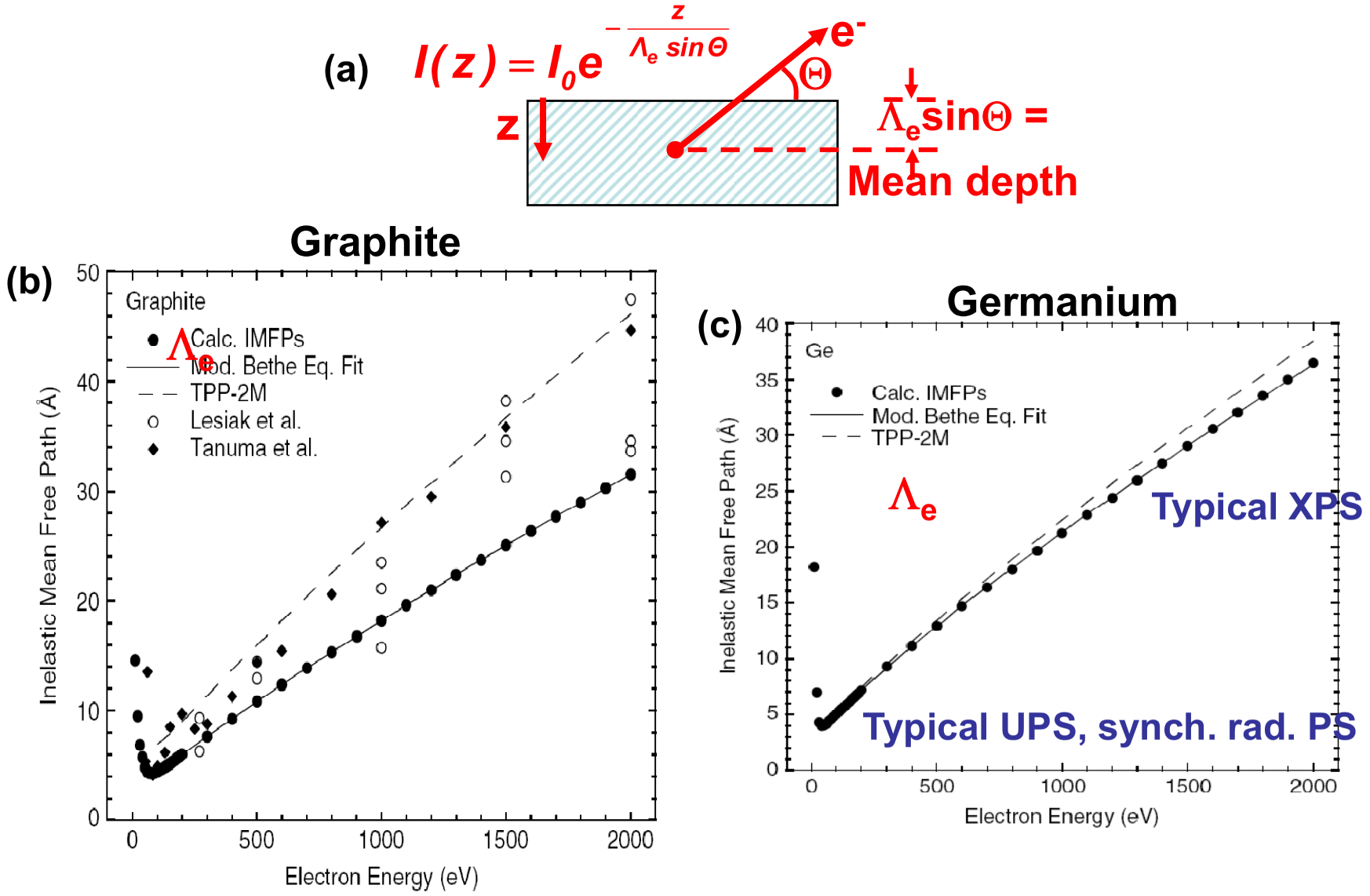

Fig. 3

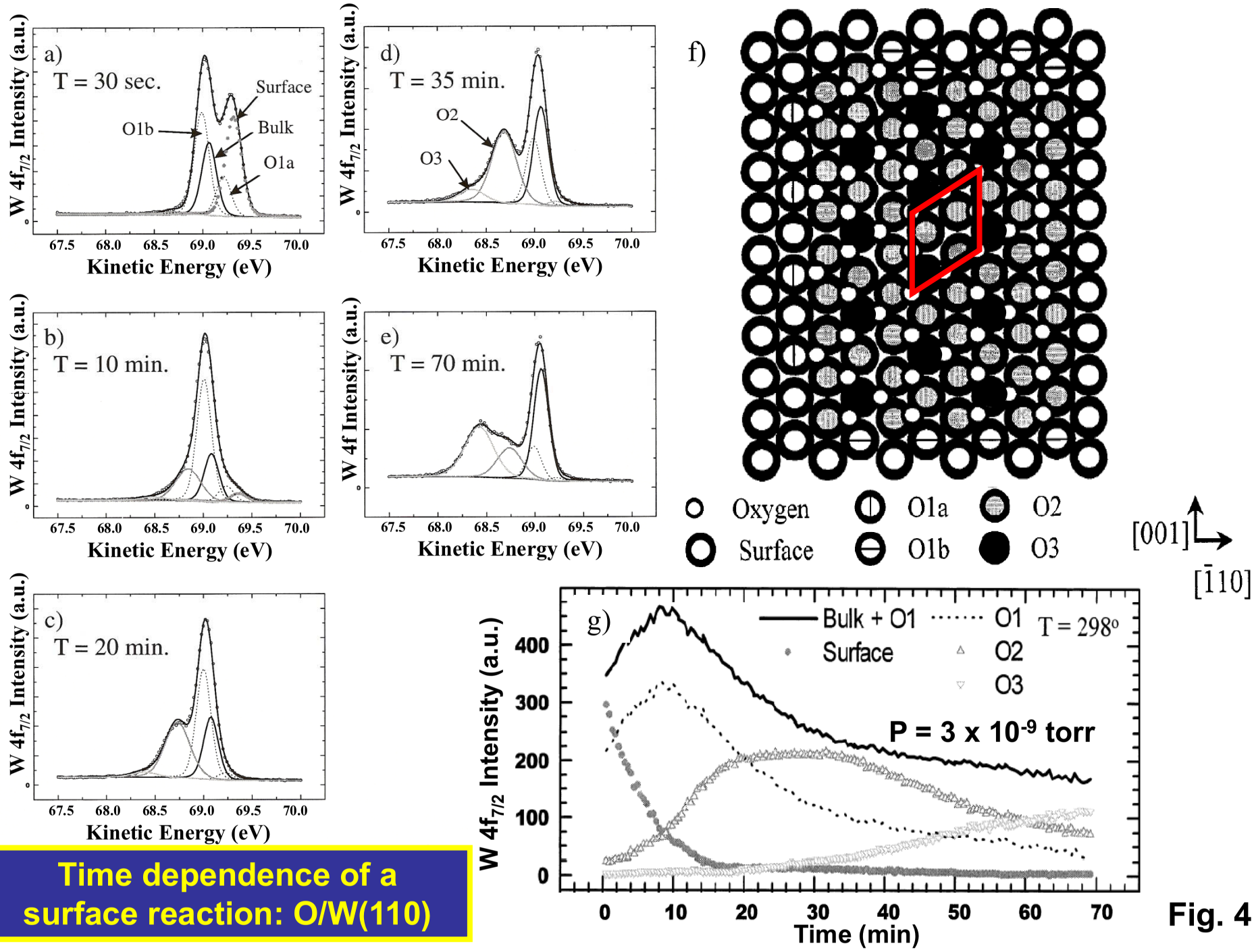

Time dependence of a surface reaction: O/W(110)

Fig. 4

Temperature dependence of Mn3s and O1s spectra: $La_{0.7}Sr_{0.3}MnO_3$

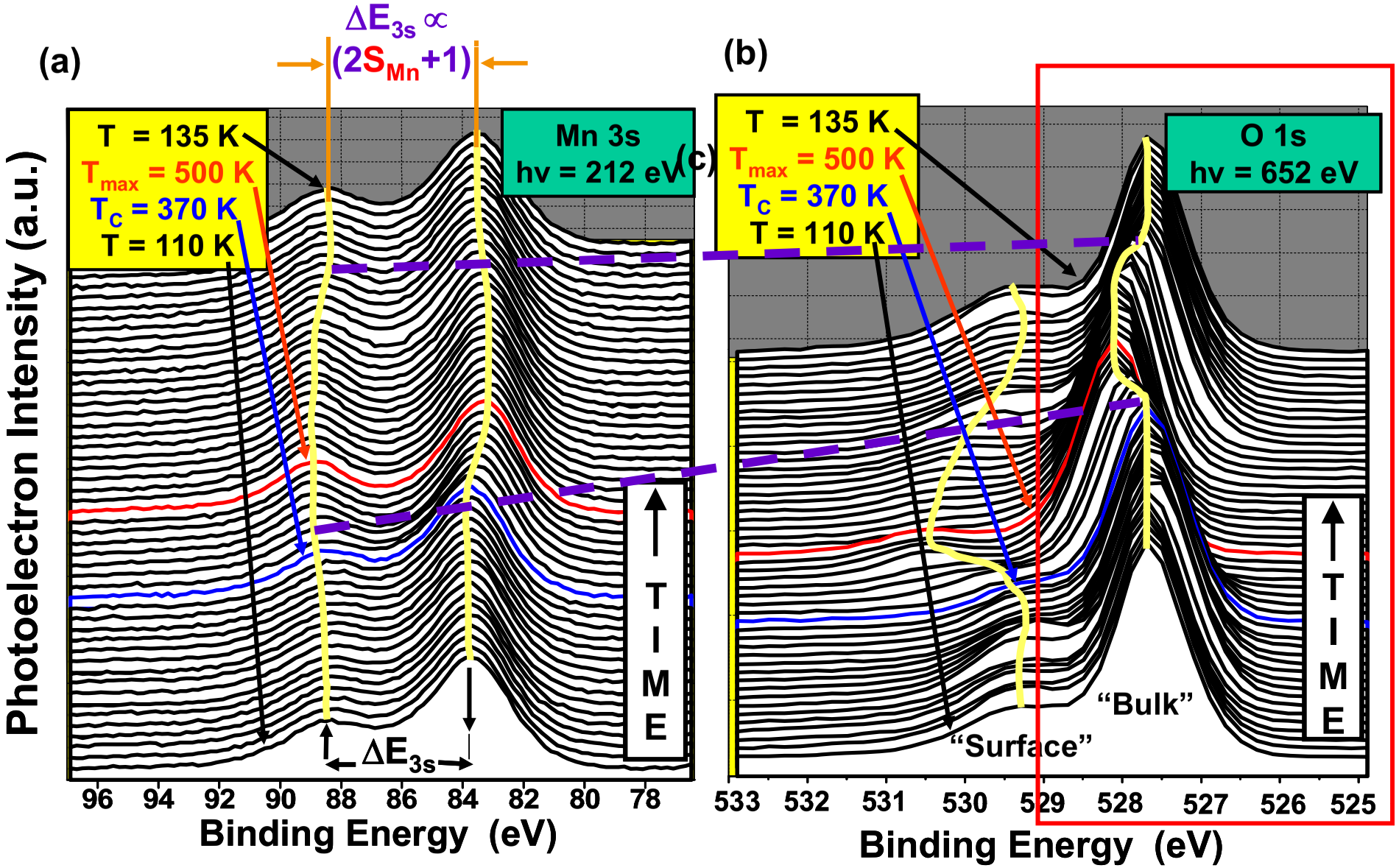

Fig. 5

Multiplet splitting in core levels of transition metal compounds

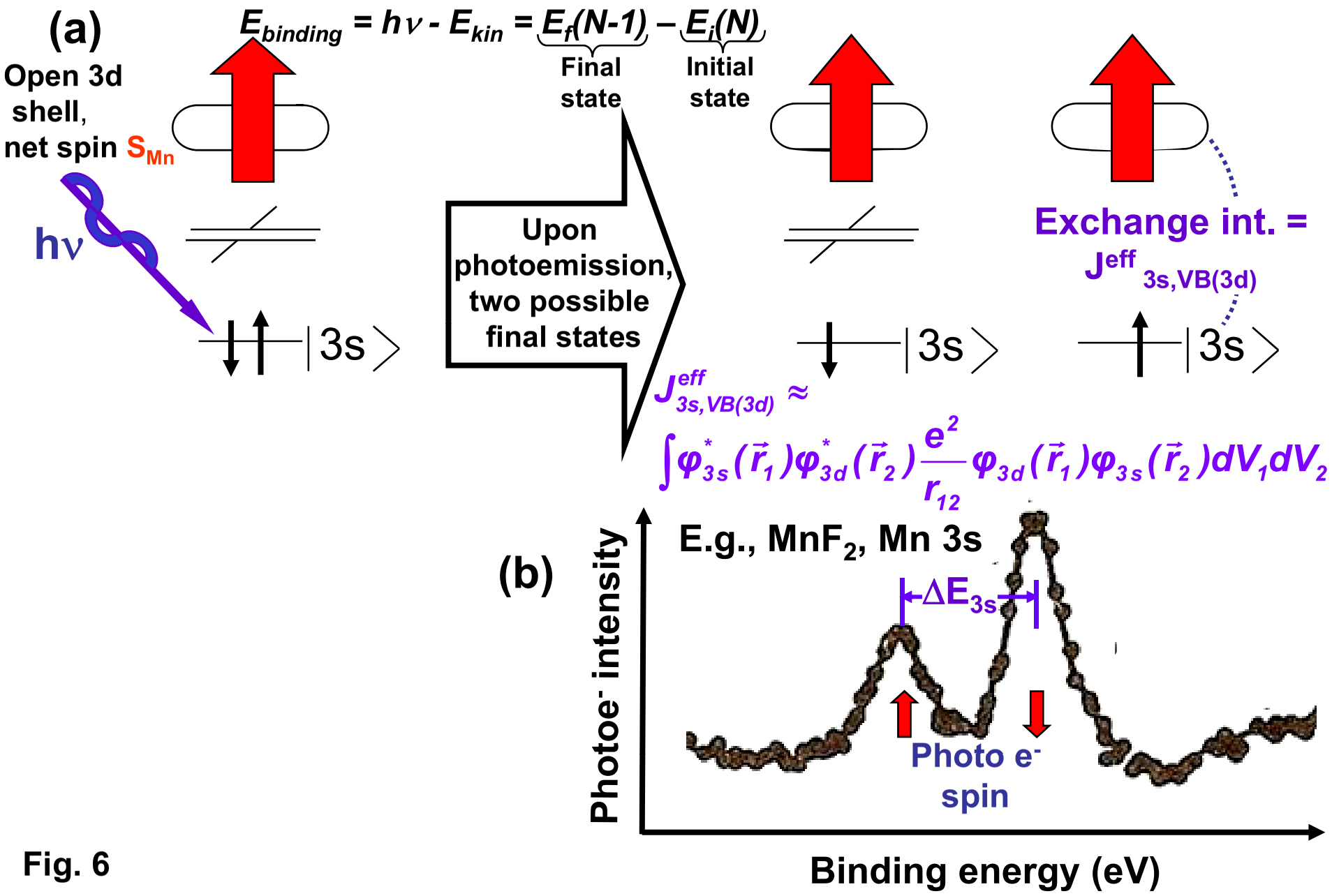

Fig. 6

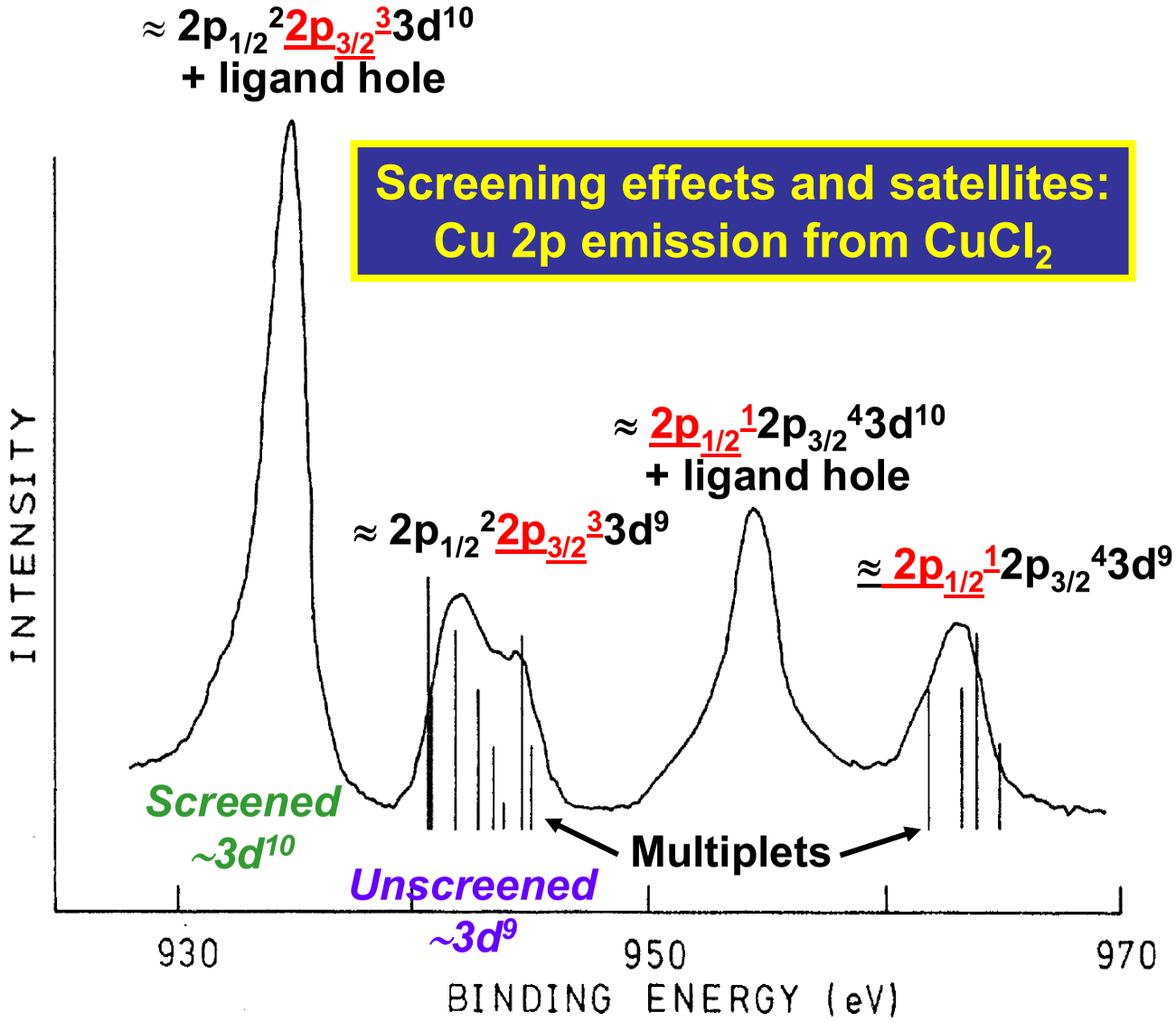

$$\Psi_{final,K}(N-1) = C_{1,K}(2p^2_{1/2}\,2p^3_{3/2}\,3d^{10} + C\ell\ hole) + C_{2,K}(2p^2_{1/2}\,2p^3_{3/2}\,3d^9)$$

Fig. 7

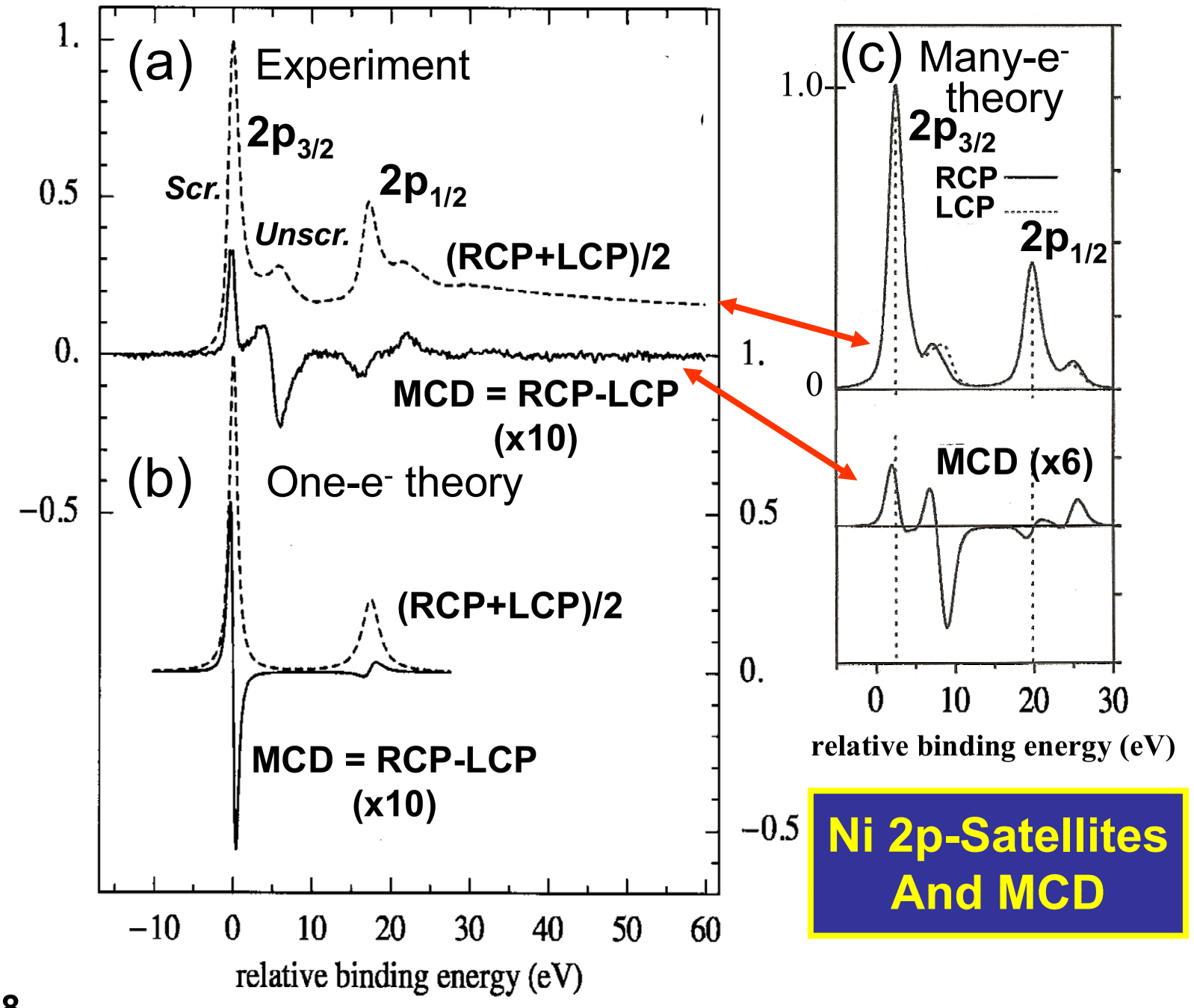
(a) Experiment
2p3/2
2p1/2
Scr.
Unscr.
(RCP+LCP)/2
MCD = RCP-LCP
(x10)
(b) One-e- theory
(RCP+LCP)/2
MCD = RCP-LCP
(x10)
relative binding energy (eV)
(c) Many-e- theory
2p3/2
RCP
LCP
2p1/2
MCD (x6)
relative binding energy (eV)
Ni 2p-Satellites
And MCD

Fig. 8

1st Expt. Magnetic Circular Dichroism 1-e- Theo.

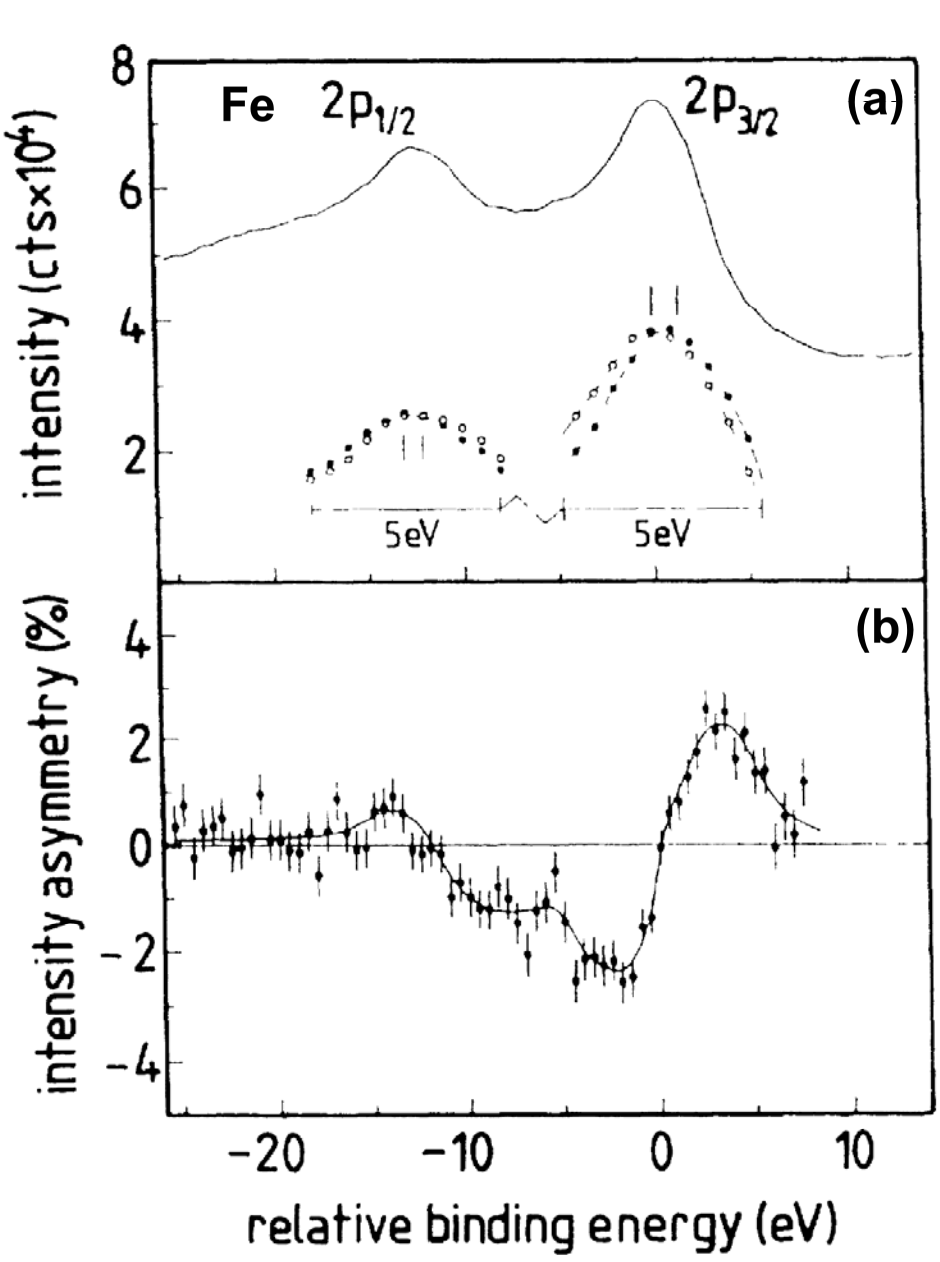

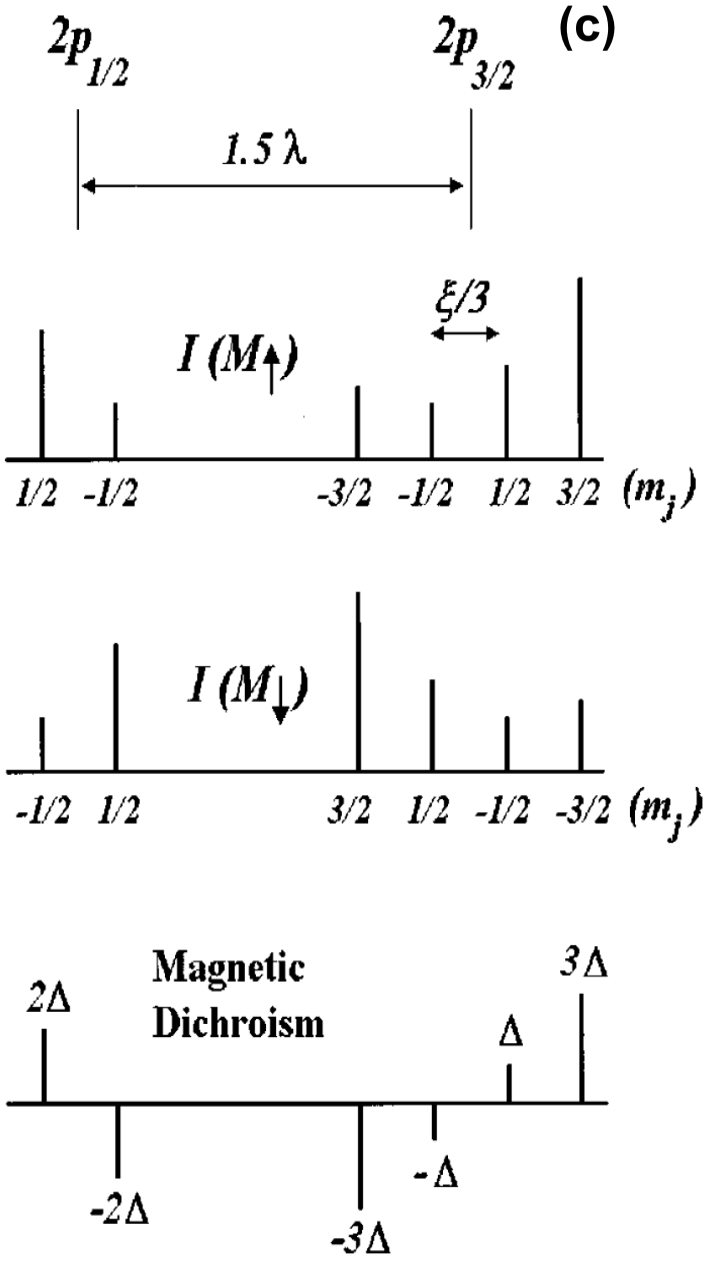

Fig. 9

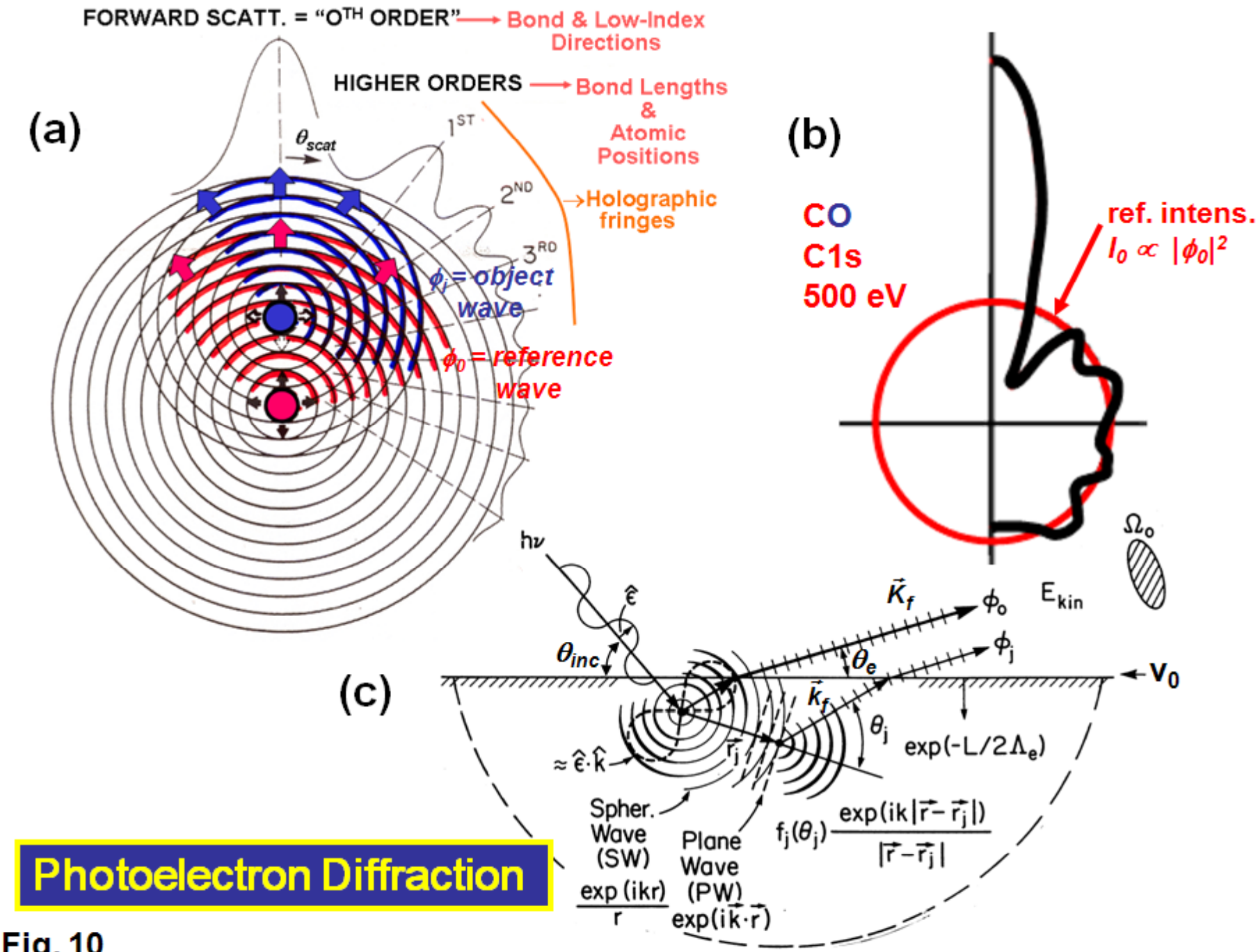

Photoelectron Diffraction

Fig. 10

X-ray Photoelectron Diffraction:1ML FeO on Pt(111)

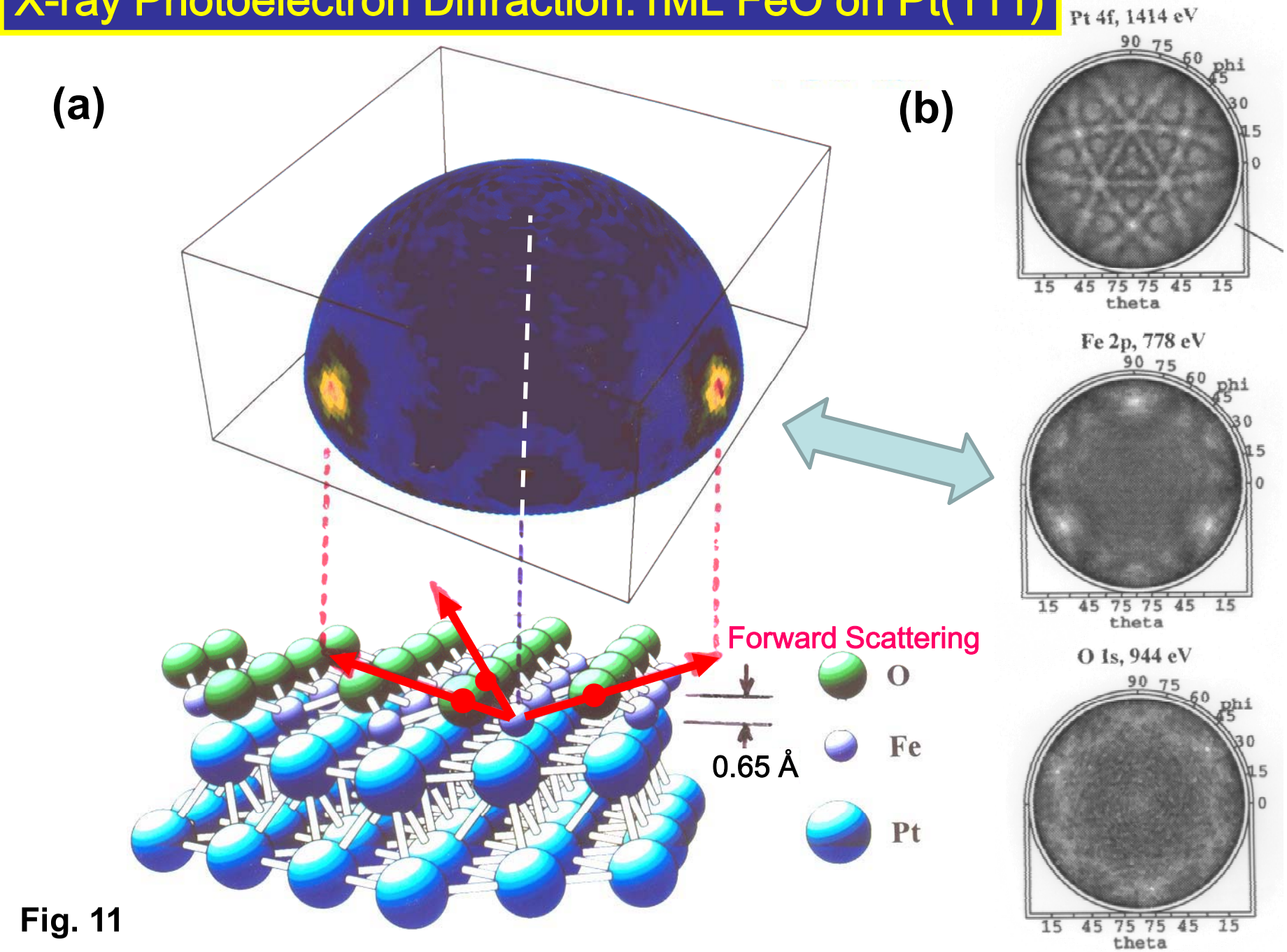

Fig. 11

Differential photoelectron holography in Cu(001) —Cu 3p emission

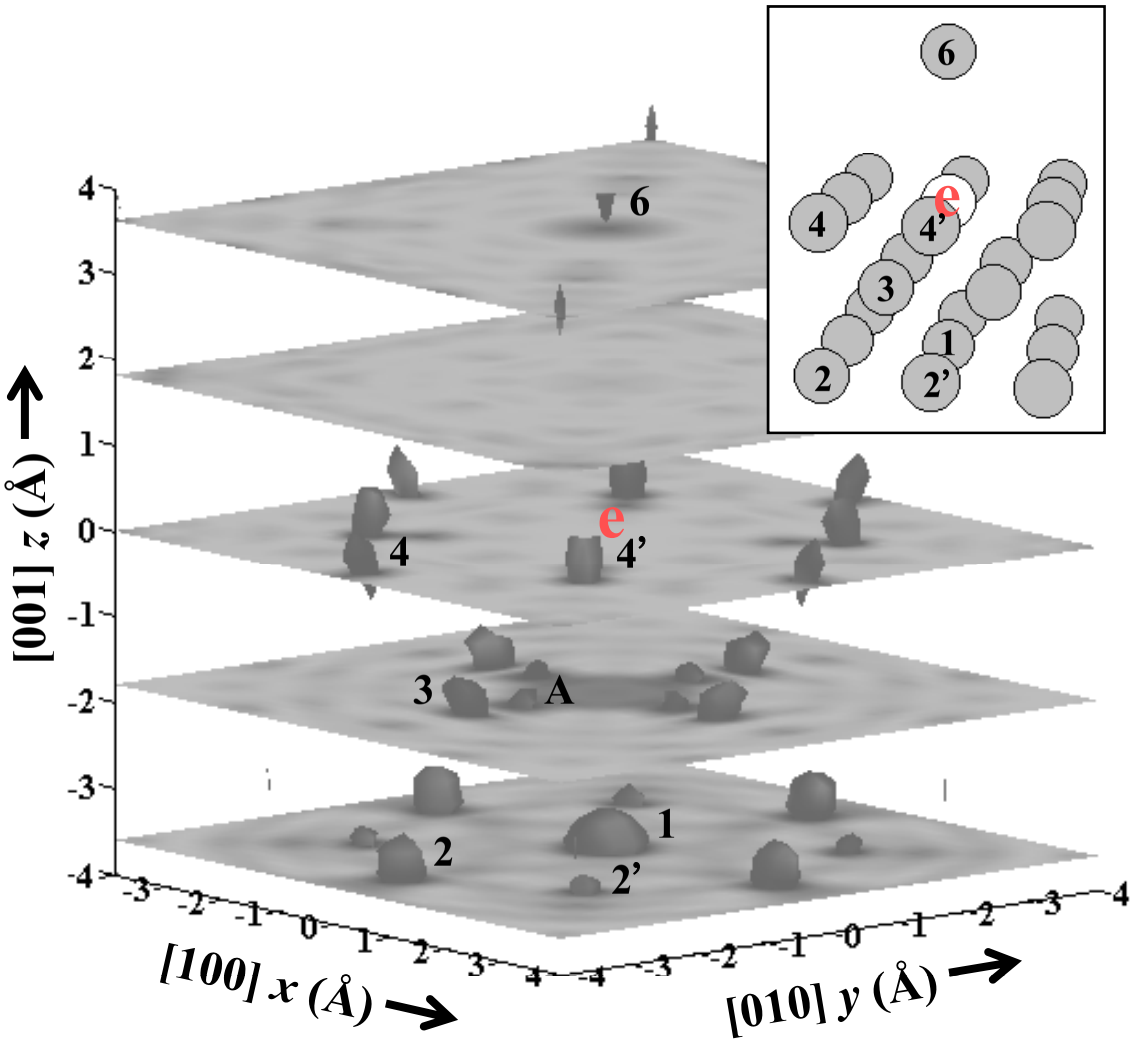

Fig. 12

Valence-band photoemission: Angle-Resolved Photoemission (ARPES)

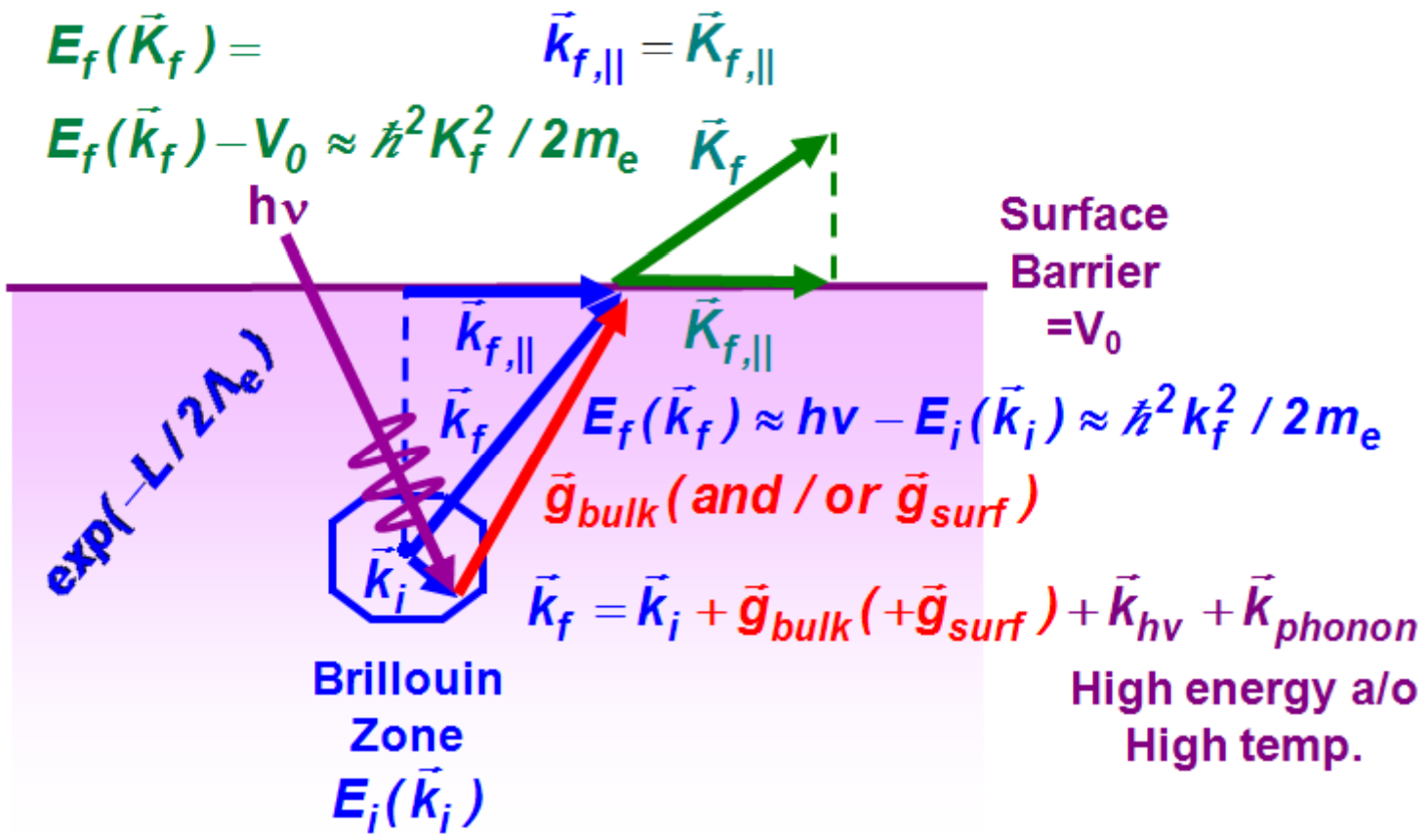

$$I(E_f, \vec{k}_f) \propto \left| \hat{\varepsilon} \bullet \left\langle \varphi_{photoe}(E_f = h\nu + E_i, \vec{k}_f = \vec{k}_i + \vec{g}) \middle| \vec{r} \middle| \varphi(E_i, \vec{k}_i) \right\rangle \right|^2$$

"Direct" or k-conserving transitions

Fig. 13

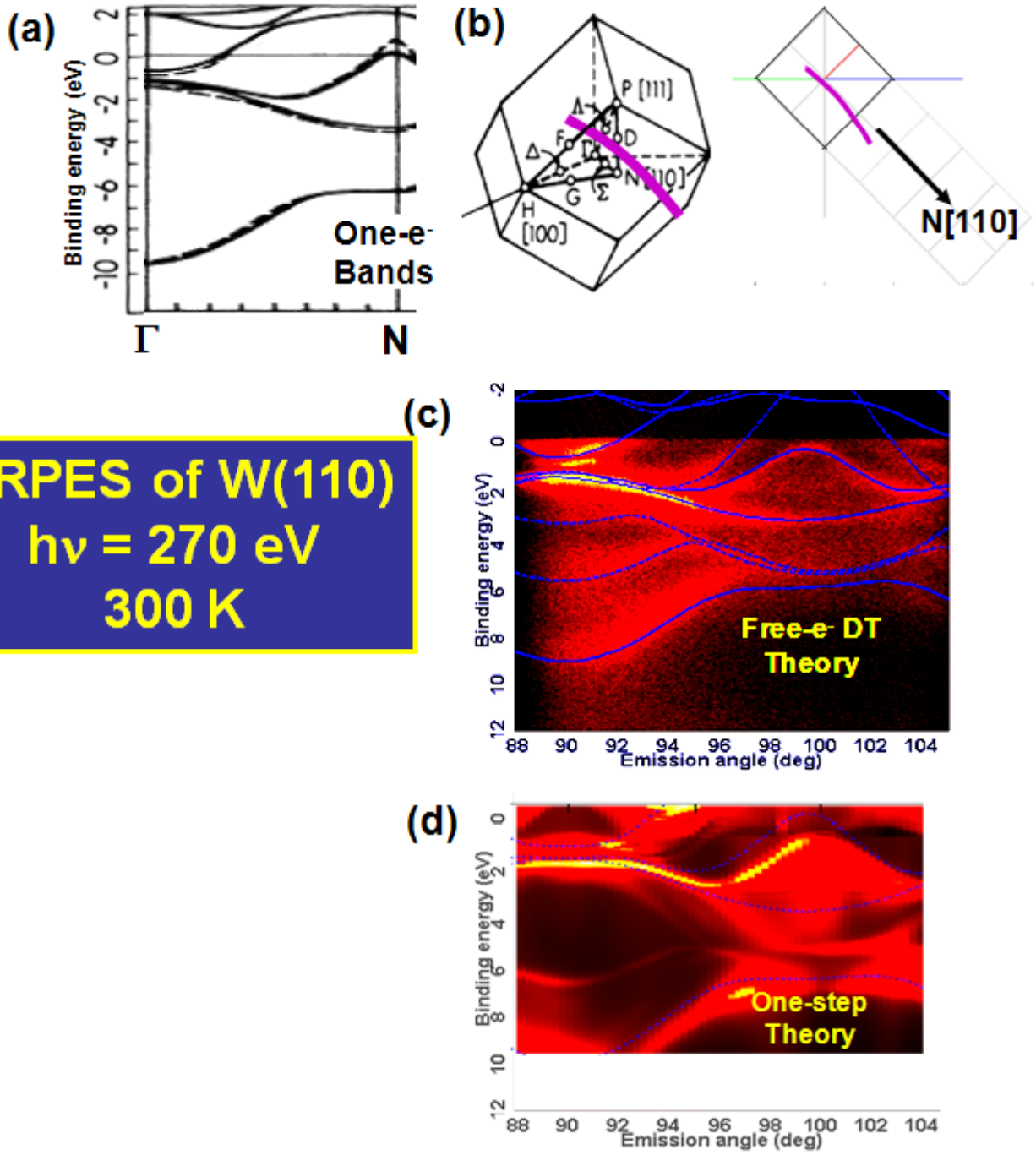
(a)
Binding energy (eV)
2
0
-2
-4
-6
-8
-10
One-e⁻
Bands
Γ
N
(b)
P [111]
Δ
F
D
Δ
N [110]
G
Σ
H
[100]
N[110]
ARPES of W(110)
hν = 270 eV
300 K
(c)
Free-e⁻ DT
Theory
Binding energy (eV)
0
2
4
6
8
10
12
88
90
92
94
96
98
100
102
104
Emission angle (deg)
(d)
One-step
Theory
Binding energy (eV)
0
2
4
6
8
10
12
88
90
92
94
96
98
100
102
104
Emission angle (deg)

Fig. 14

ARPES of Ni(111) hν = 21.2 eV

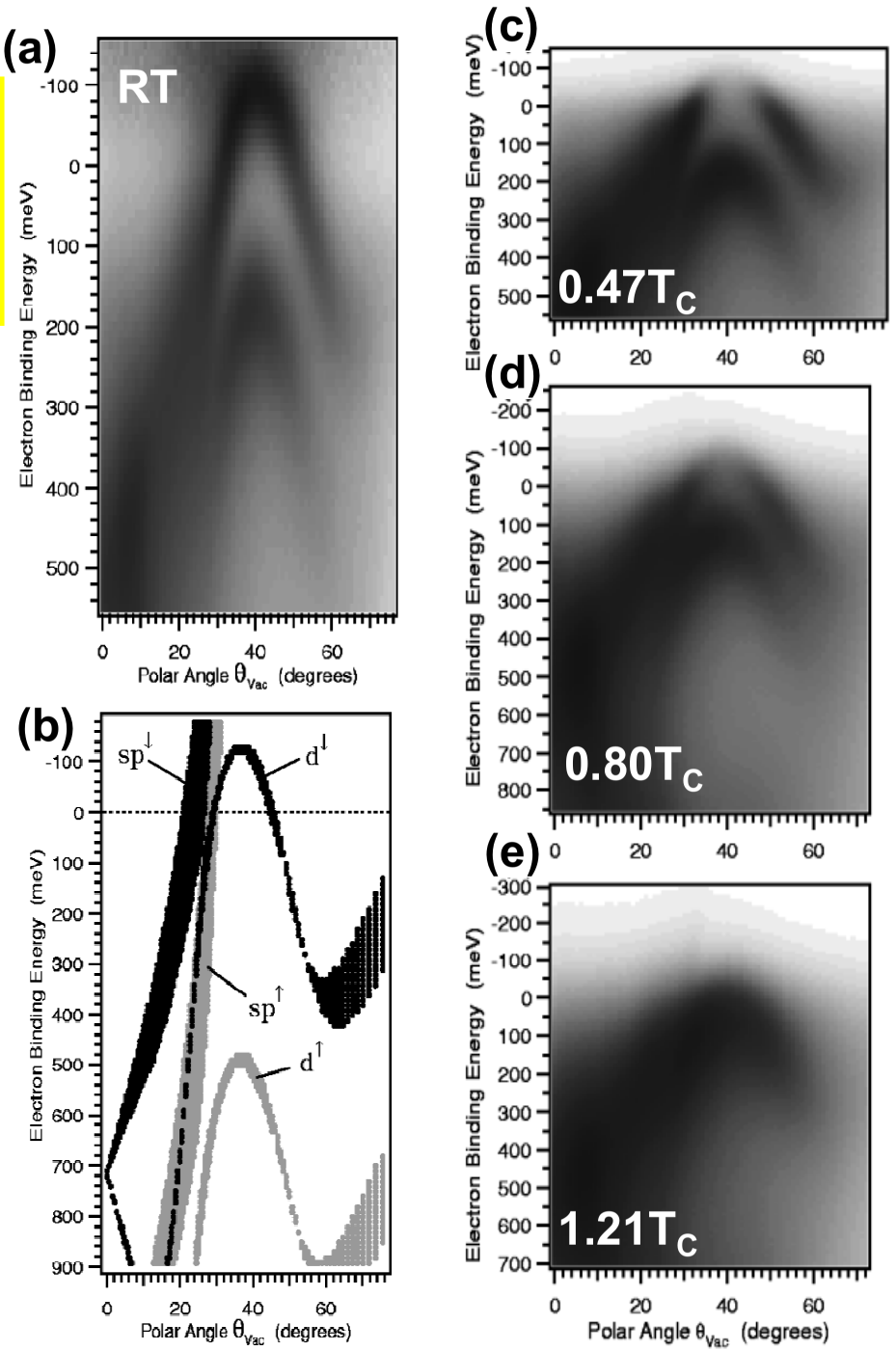

Fig. 15

XPS and HXPS in k space:

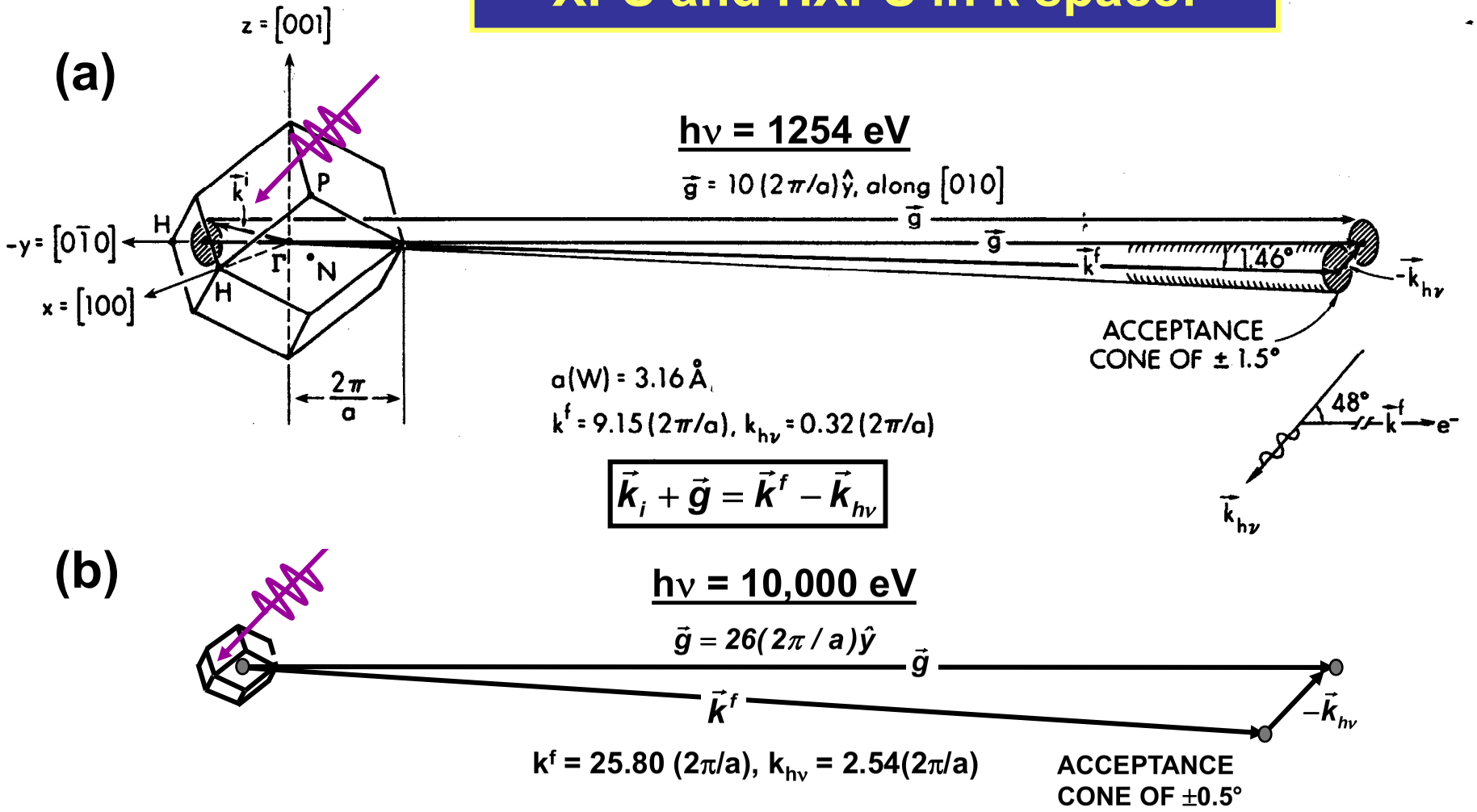

Fig. 16

(a) Gold Valence Spectrum--XPS

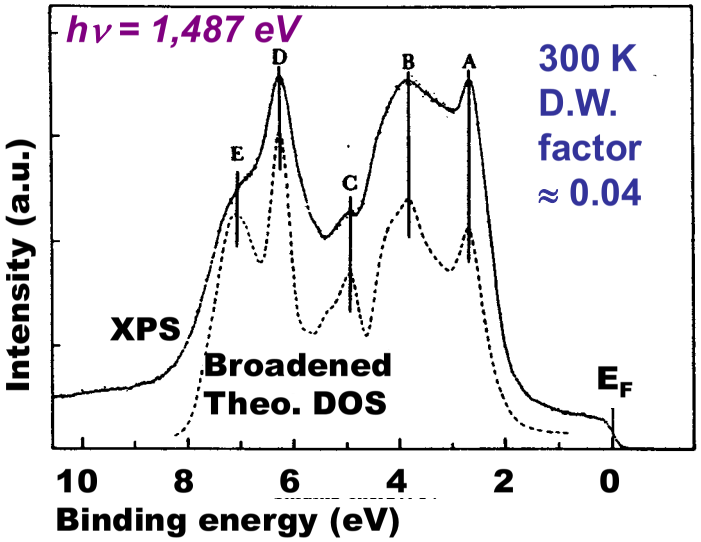

Valence spectra in the XPS Limit

(b) Gold Valence Spectrum--HXPS

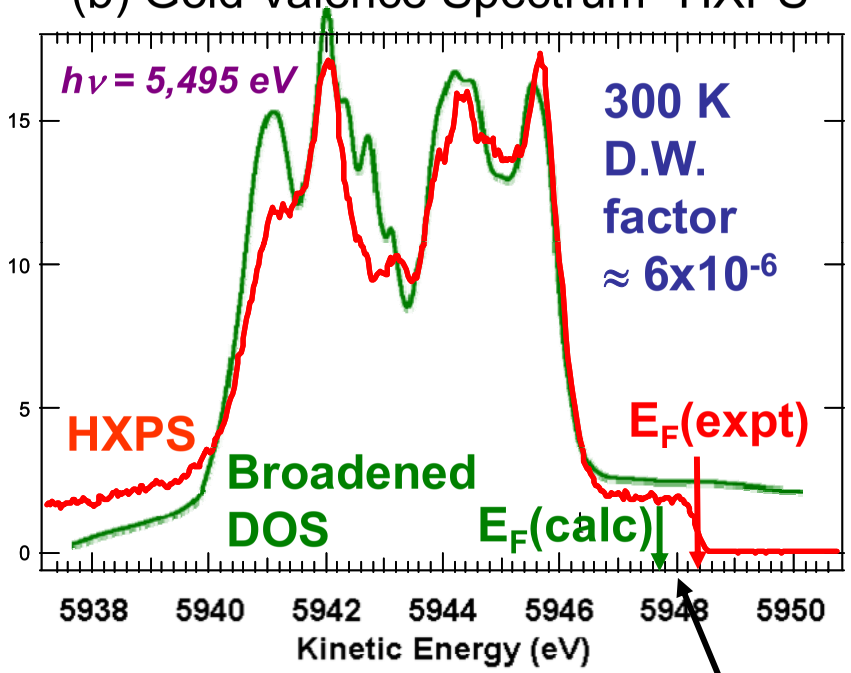

Screening/
self-energy
correction:
~0.6 eV

(c) Silver Valence Spectrum--XPS

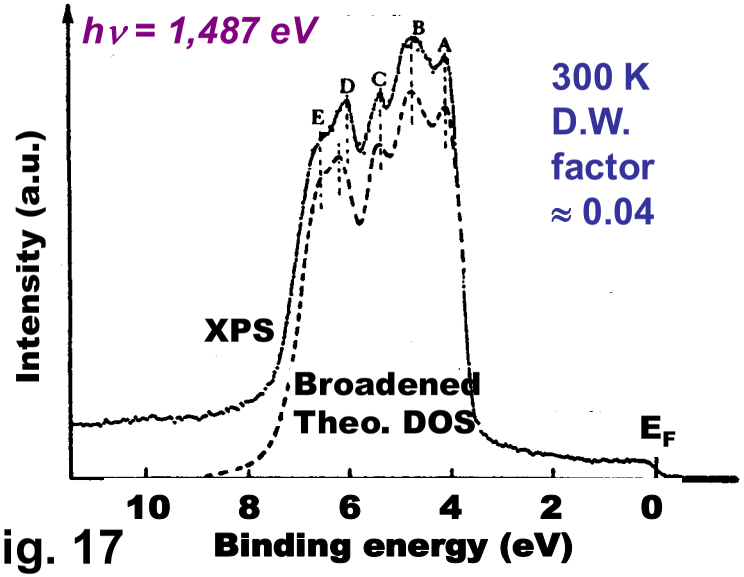

Fig. 17

ARPES from W(110): Expt, hν = 860 eV, near-normal emission, Θ_{Debye} = 400K

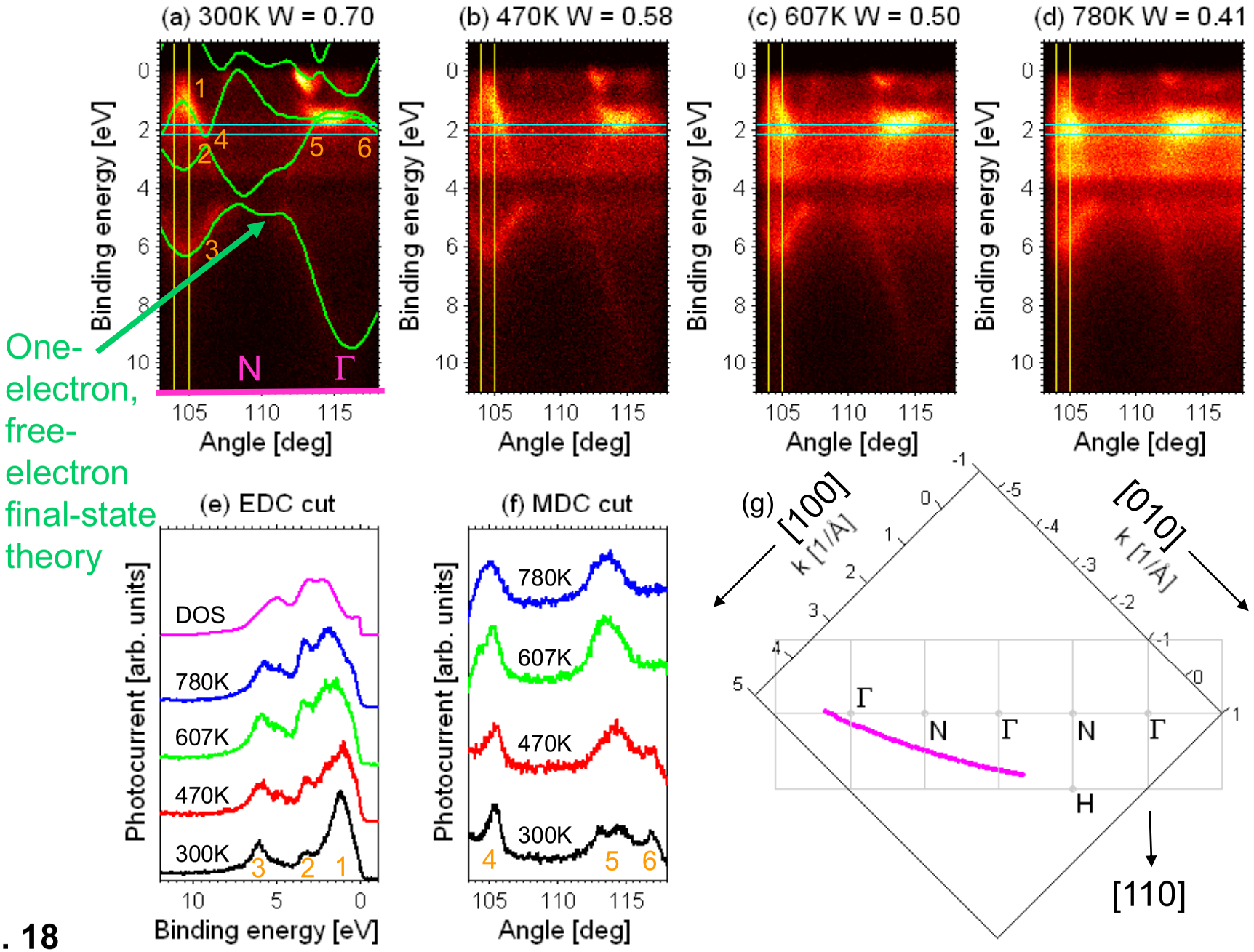

Fig. 18

Variable takeoff-angle Si 1s photoelectron spectra from NiGe(12-nm)/SiO_2(12-nm)/Si(100)

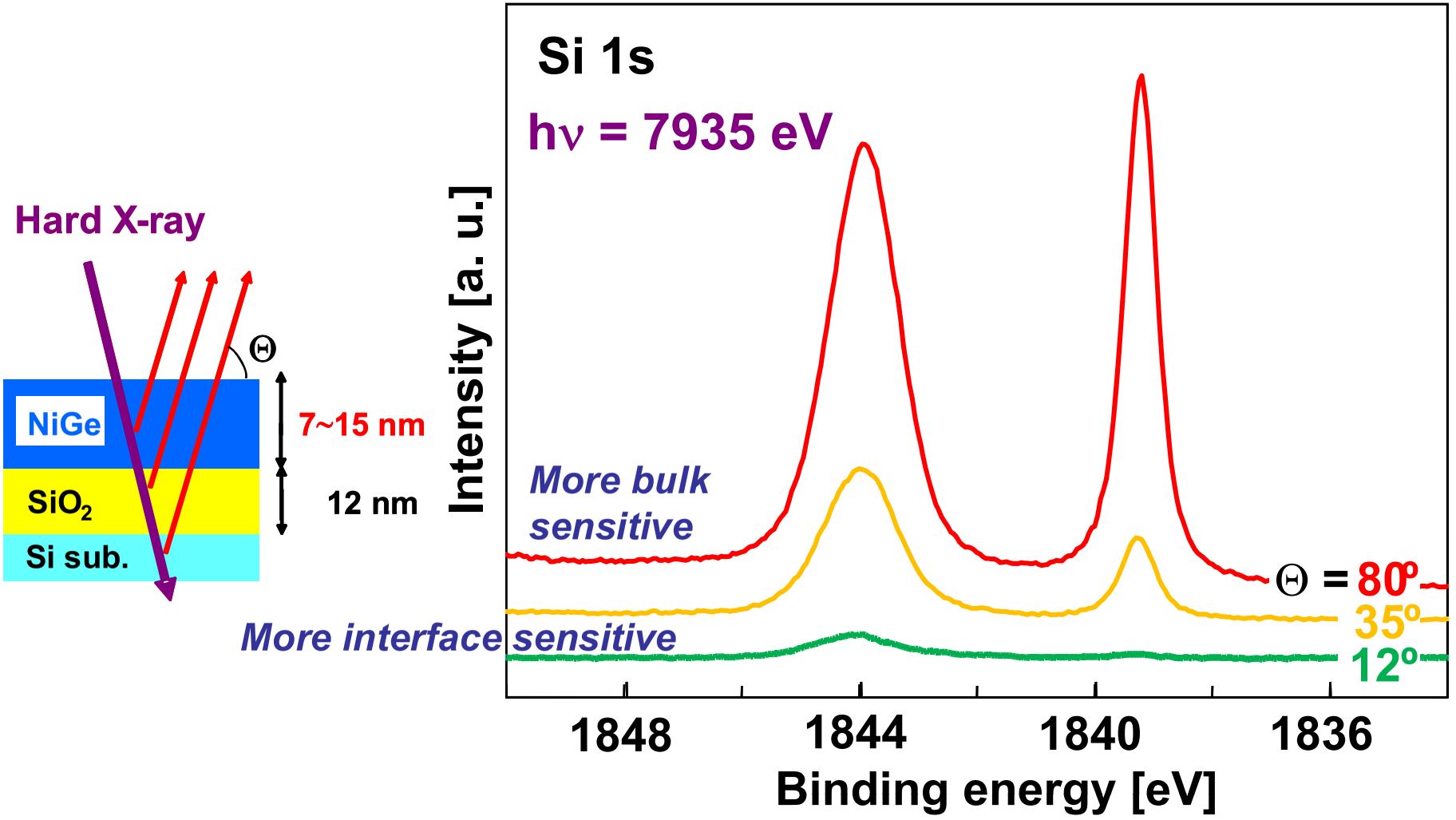

Fig. 19

Satellite structure in HXPS core-level spectra of strongly correlated materials: Mn 2p of $La_{0.7}Sr_{0.3}MnO_3$

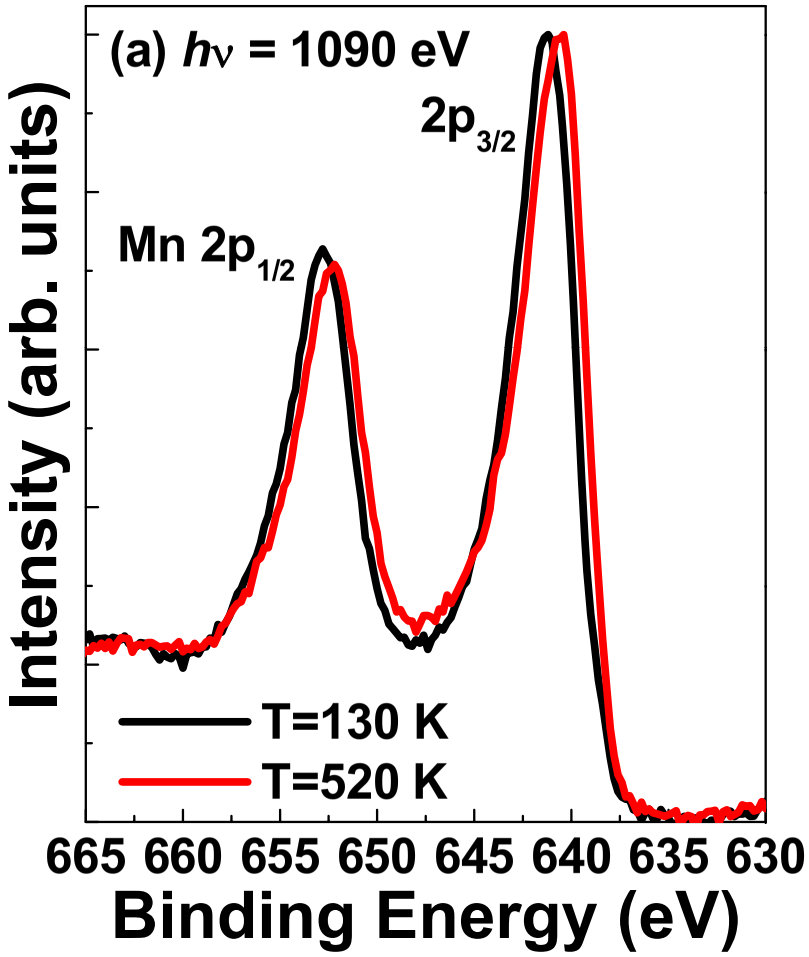

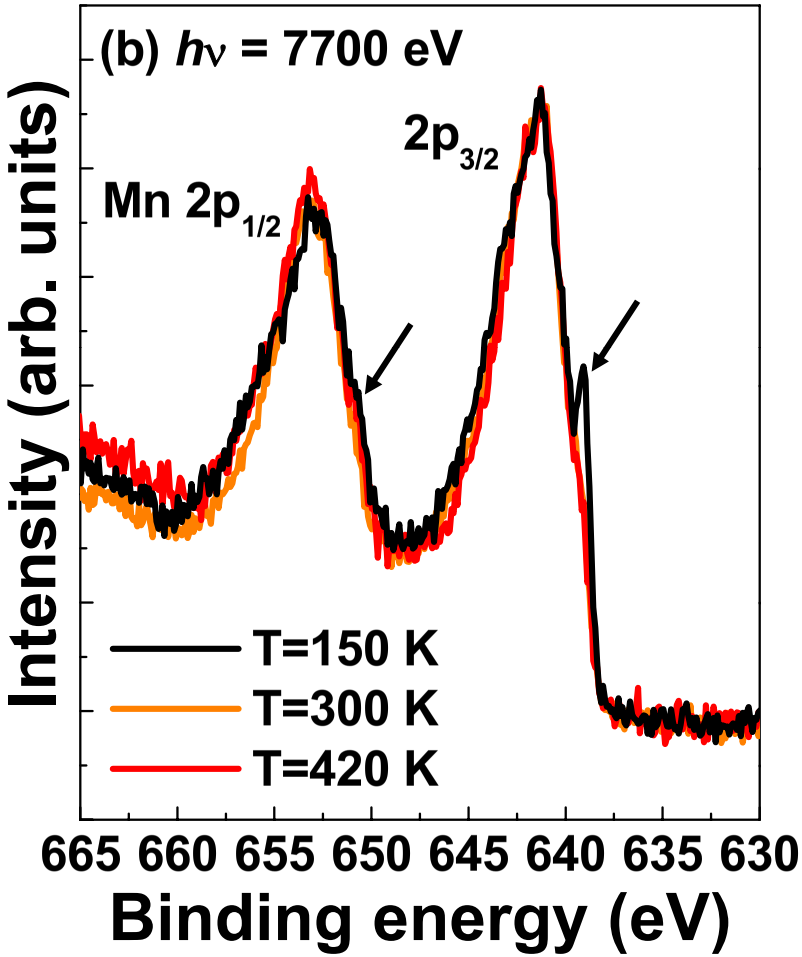

Fig. 20

Probing Buried Interfaces: The Standing Wave-Wedge ("Swedge") Method

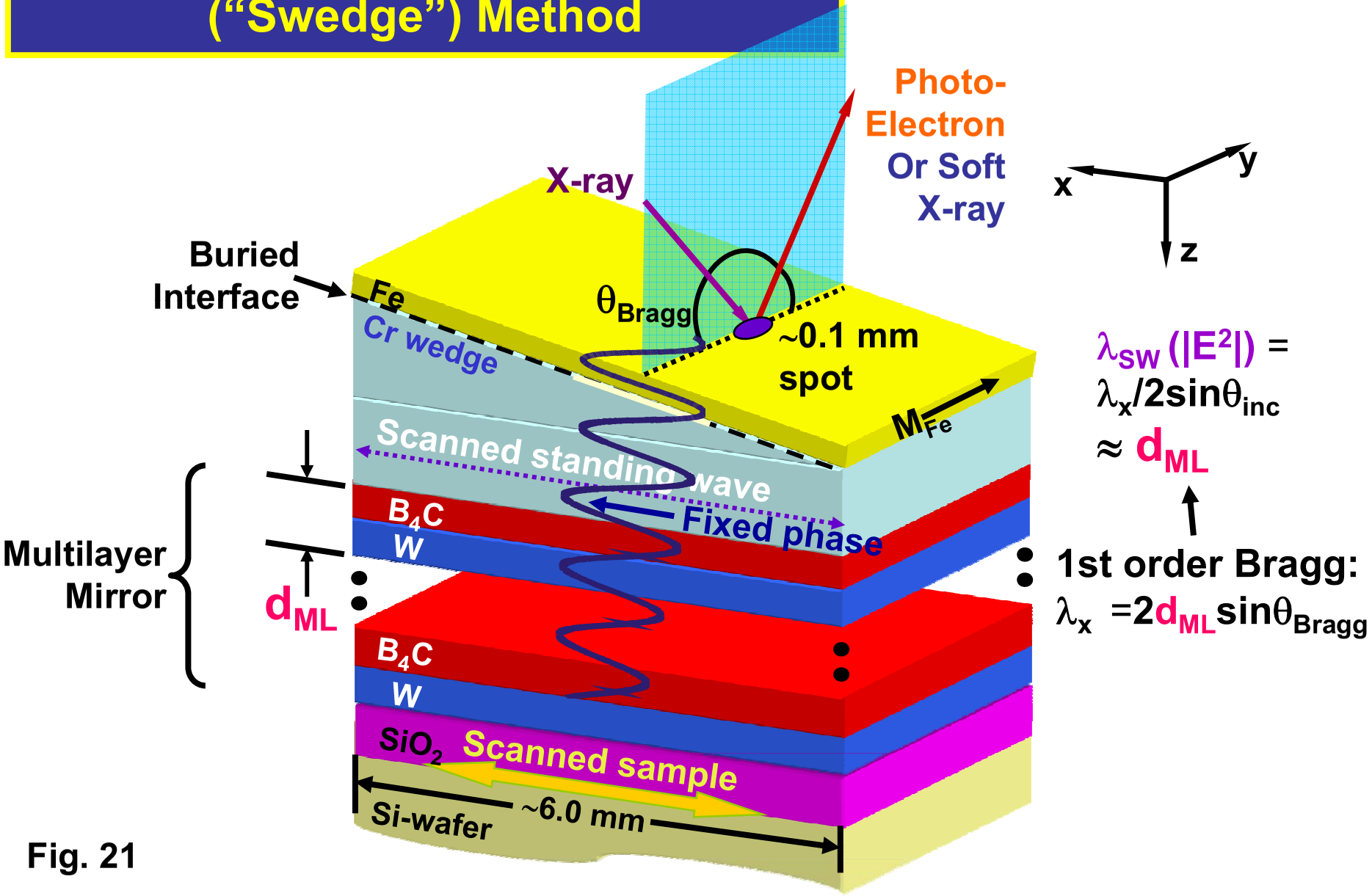

Fig. 21

Experimental + Calculated Photoemission Yield Ratio I(Cr 3p)/I(Fe3p) from Fe/Cr wedge on standing-wave multilayer

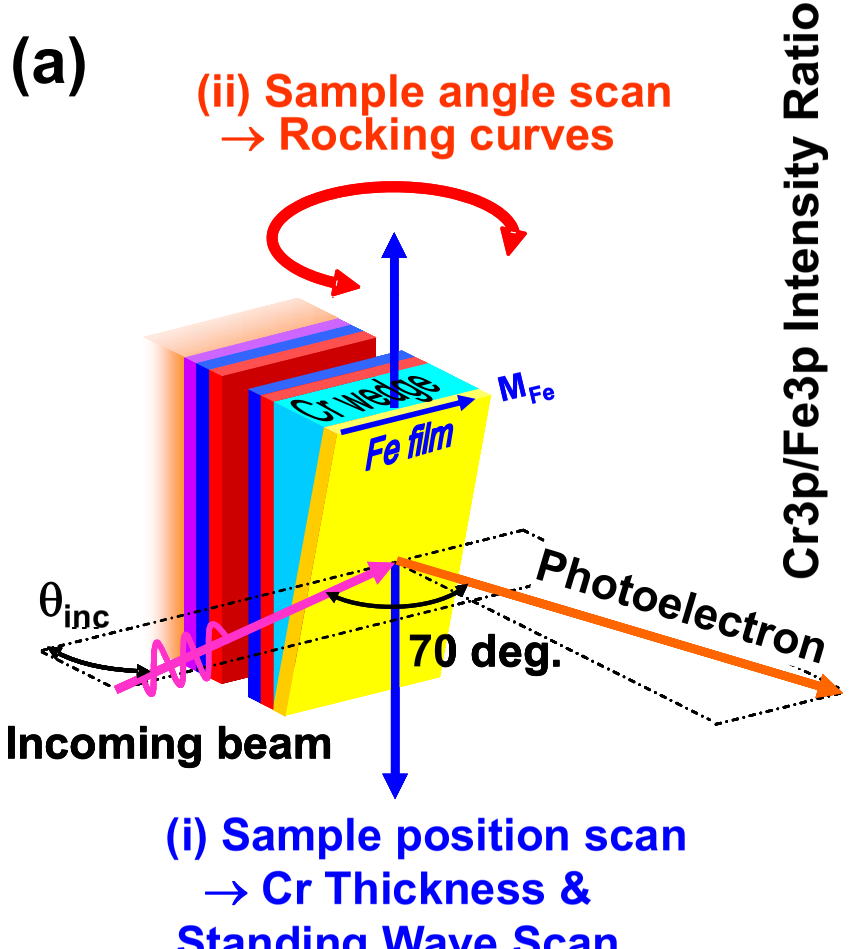

(b) Sample pos'n. scan--Standing wave scan

(c) Sample angle scan--Rocking curves

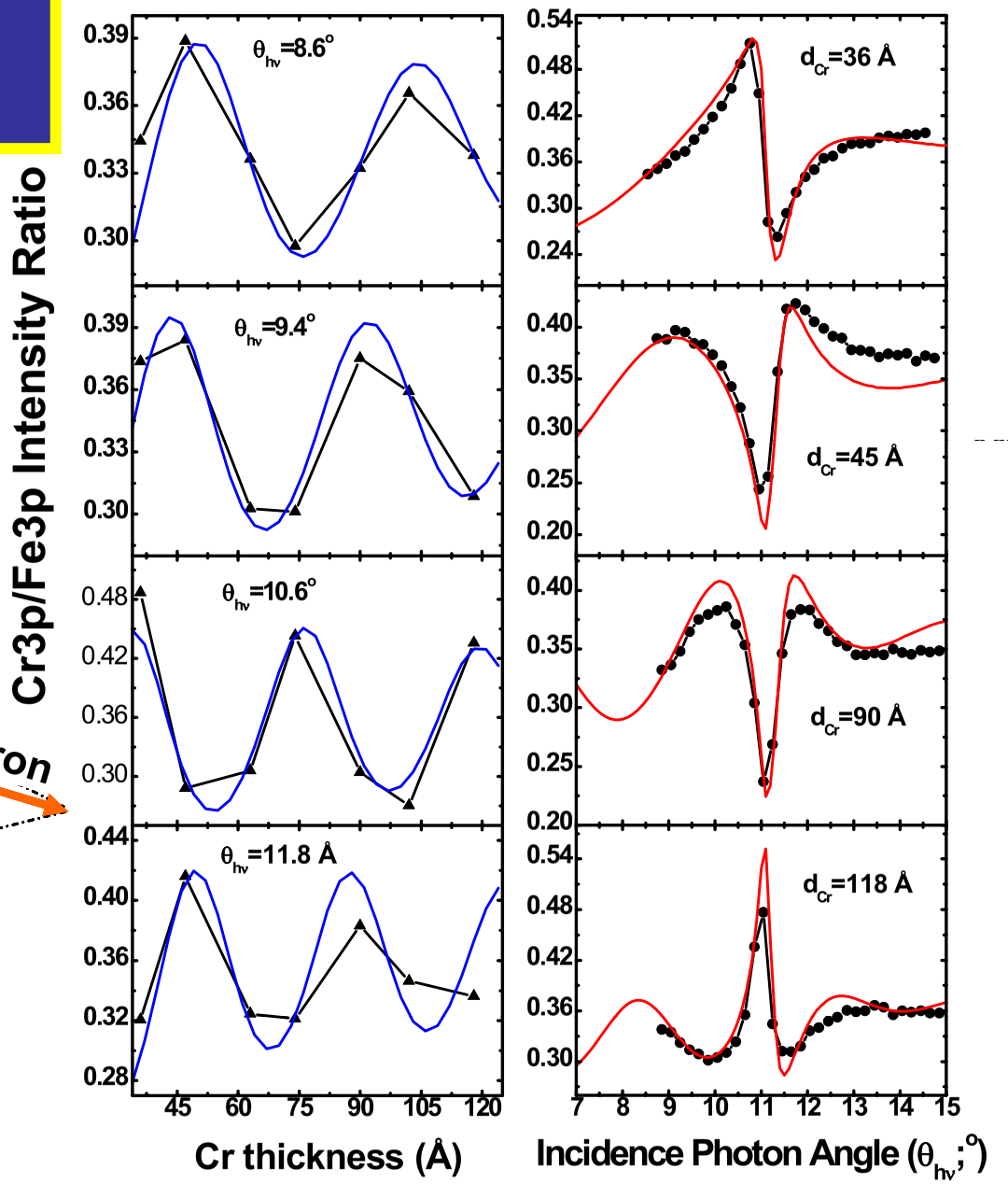

Fig. 22

Fe and Cr 2p magnetic circular dichroism--probe of y-axis magnetization

Cr magnetization Is antiparallel to Fe; systematic variation of MCD strengths vs d_{cr}

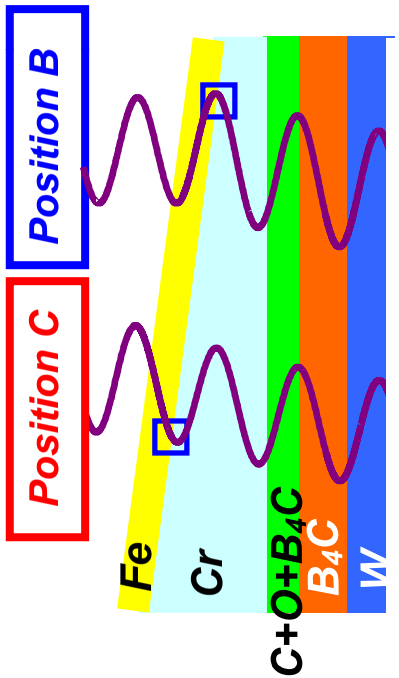

Fe and Cr 2p MCD data from Fe/Cr wedge/multilayer

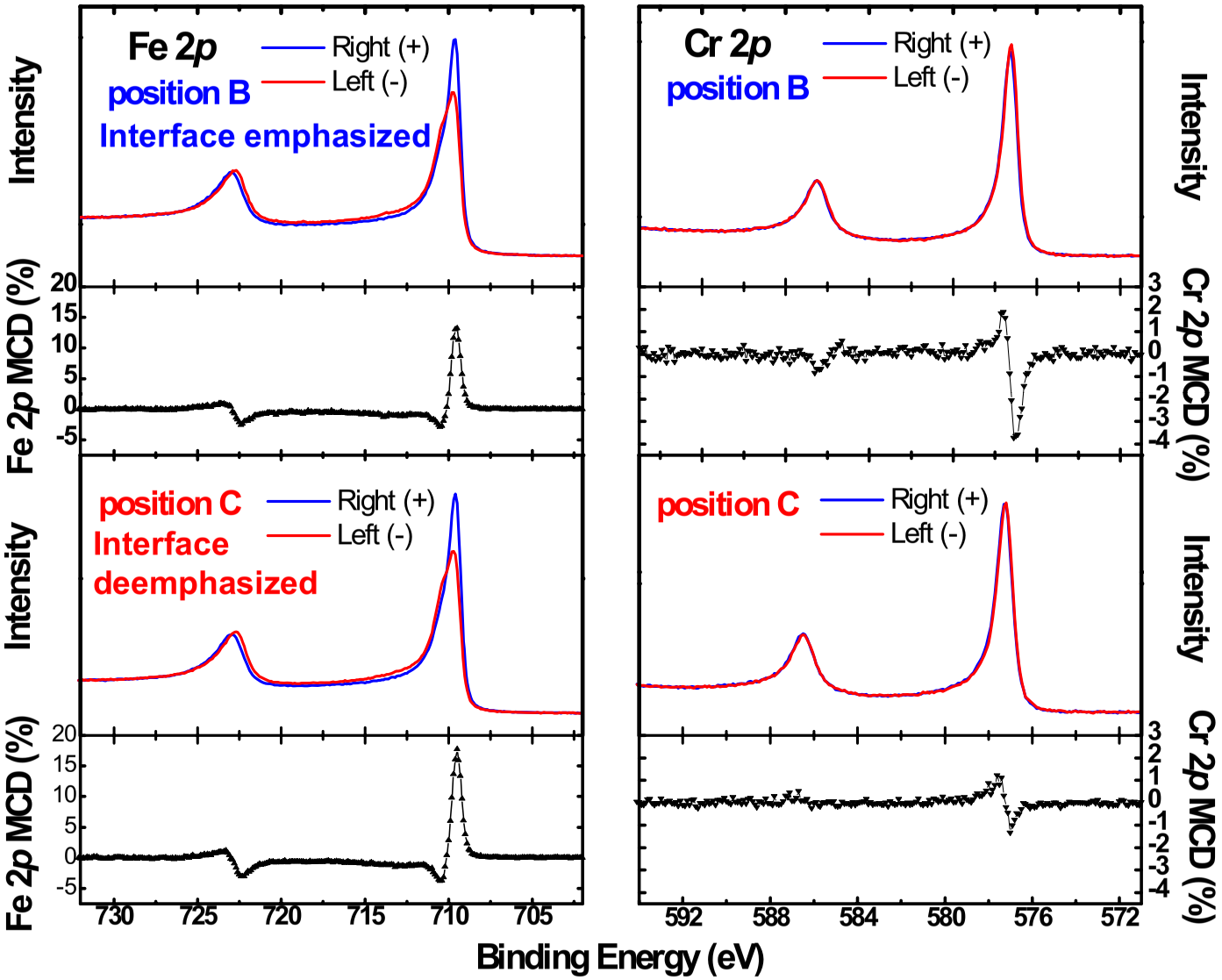

Plus similar results for Fe 3p and Cr 3p

Fig. 23

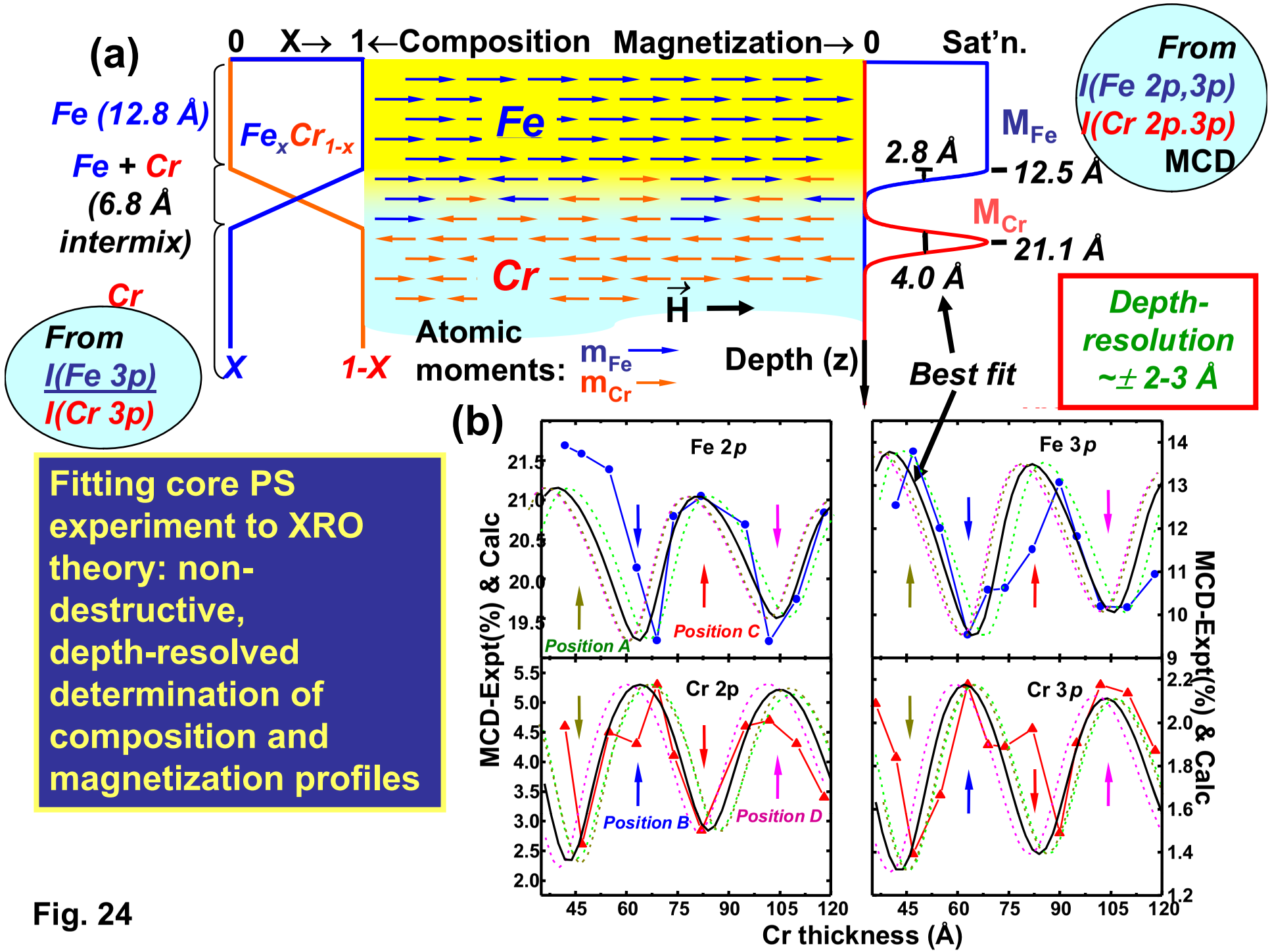
(a)
0 X→ 1←Composition Magnetization→ 0 Sat'n.
Fe (12.8 Å)
Fe + Cr
(6.8 Å
intermix)
Cr
X
1-X
Fe
Cr
H
Atomic
moments:
Depth (z)
2.8 Å
12.5 Å
4.0 Å
21.1 Å
Best fit
From
I(Fe 2p,3p)
I(Cr 2p.3p)
MCD
From
I(Fe 3p)
I(Cr 3p)
Depth-
resolution
~± 2-3 Å
Fitting core PS experiment to XRO theory: non-destructive, depth-resolved determination of composition and magnetization profiles
(b)
Fe 2p
Fe 3p
Cr 2p
Cr 3p
Position A
Position B
Position C
Position D
MCD-Expt(%) & Calc
Cr thickness (Å)

Fig. 24

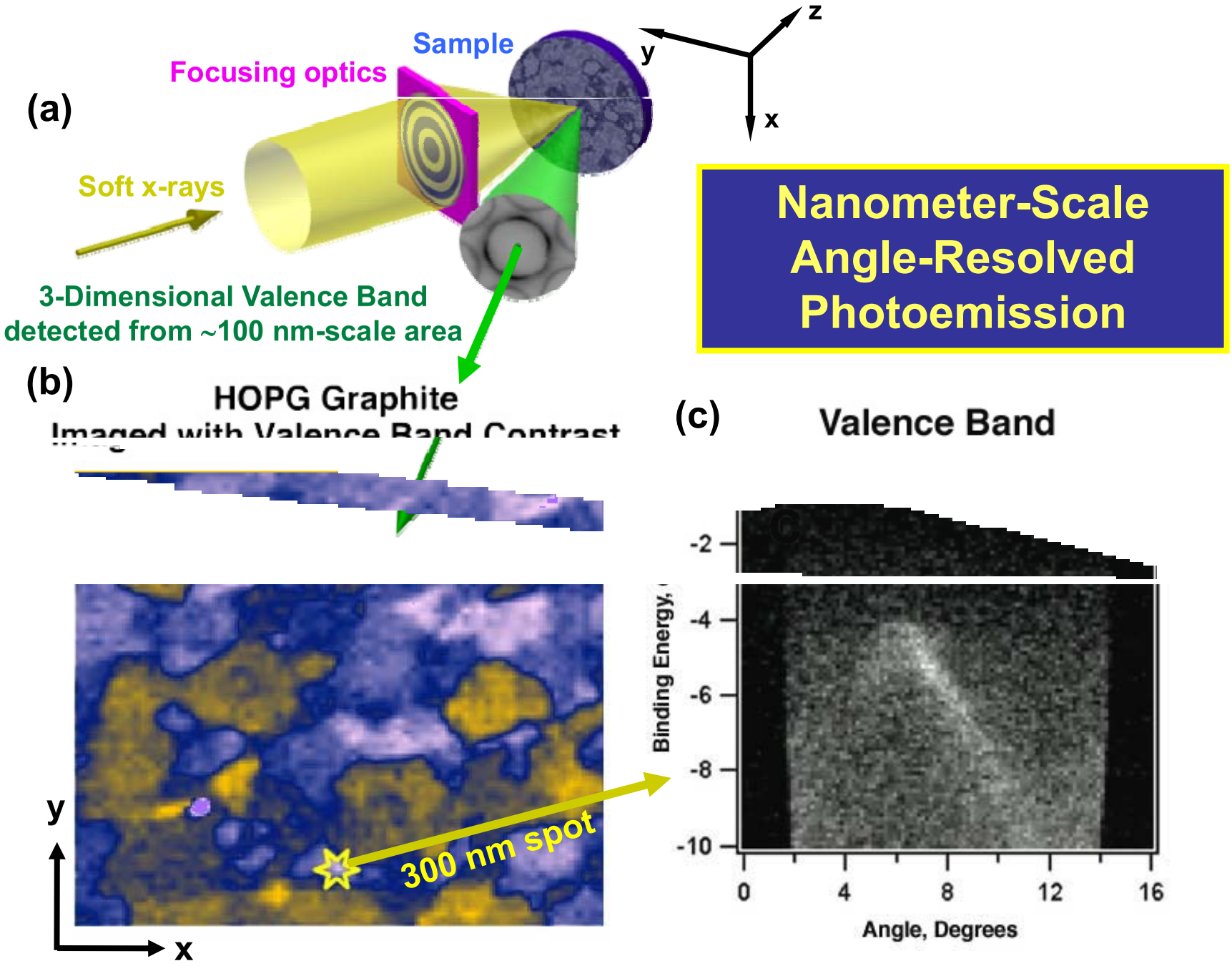
(a)
Sample
Focusing optics
Soft x-rays
z
y
x
3-Dimensional Valence Band
detected from ~100 nm-scale area
Nanometer-Scale
Angle-Resolved
Photoemission
(b)
HOPG Graphite
(c)
Valence Band
-2
-4
-6
-8
-10
Binding Energy,
0
4
8
12
16
Angle, Degrees
y
x
300 nm spot

Fig. 25

Bridging the Pressure Gap: Chemical-State- and Time- Resolved Oxidation of Si at Multi-Torr Pressures

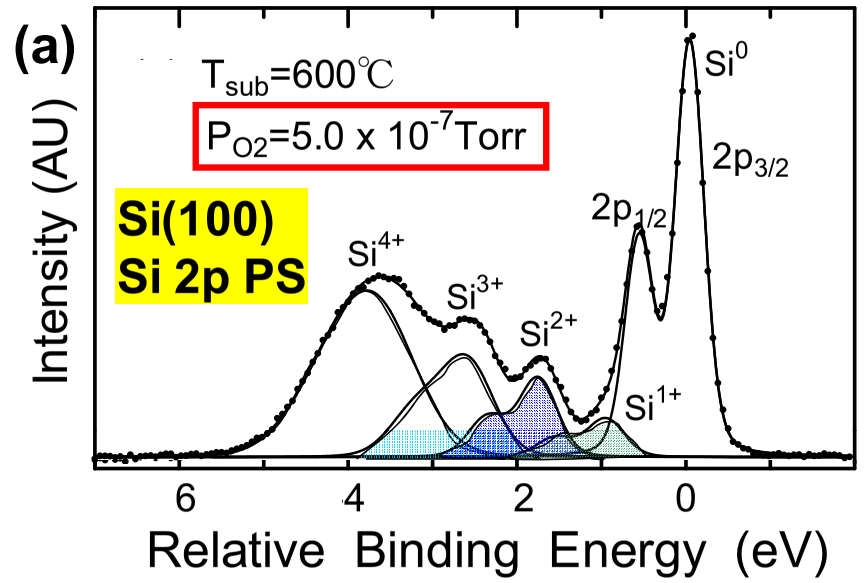

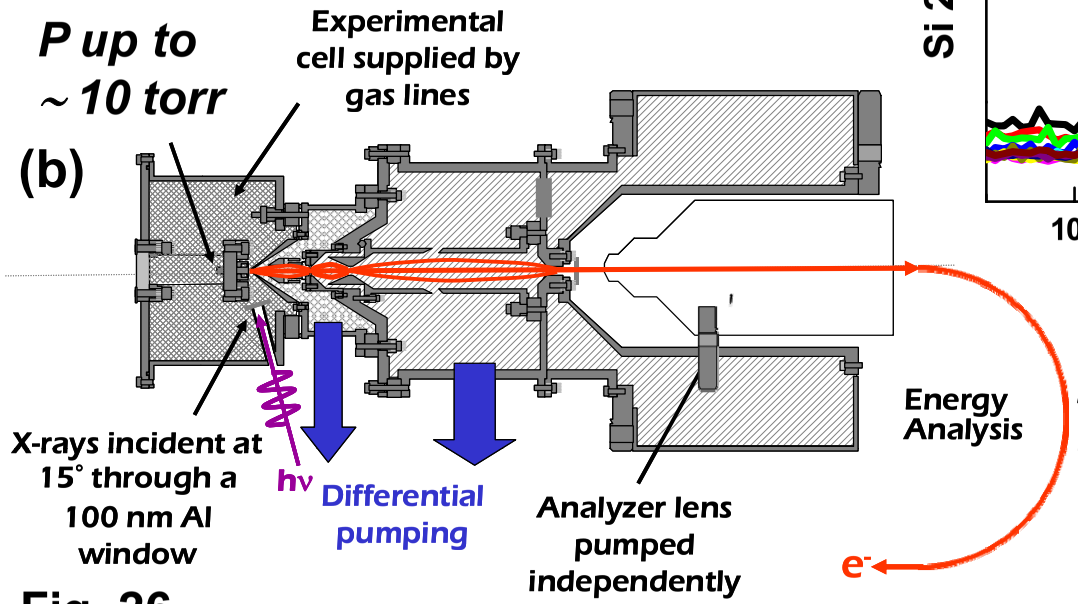

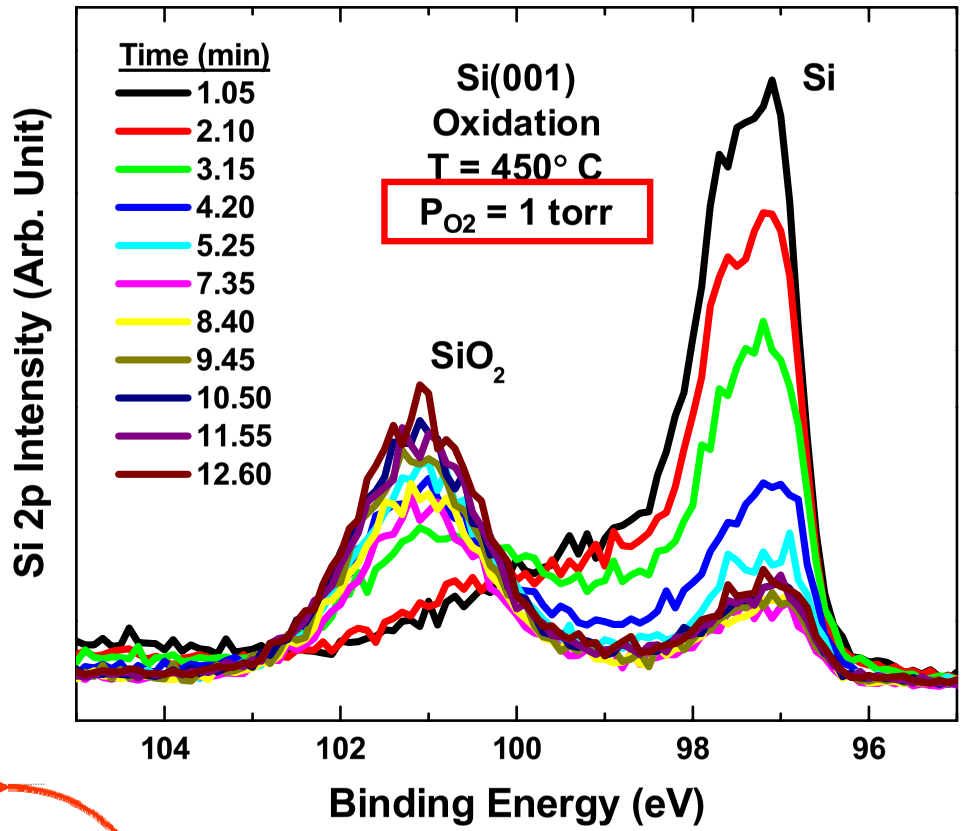

P ≈ 10^{-7} torr or better

Fig. 26

Nanoscale SiO_2 growth in real time: constant P, variable T

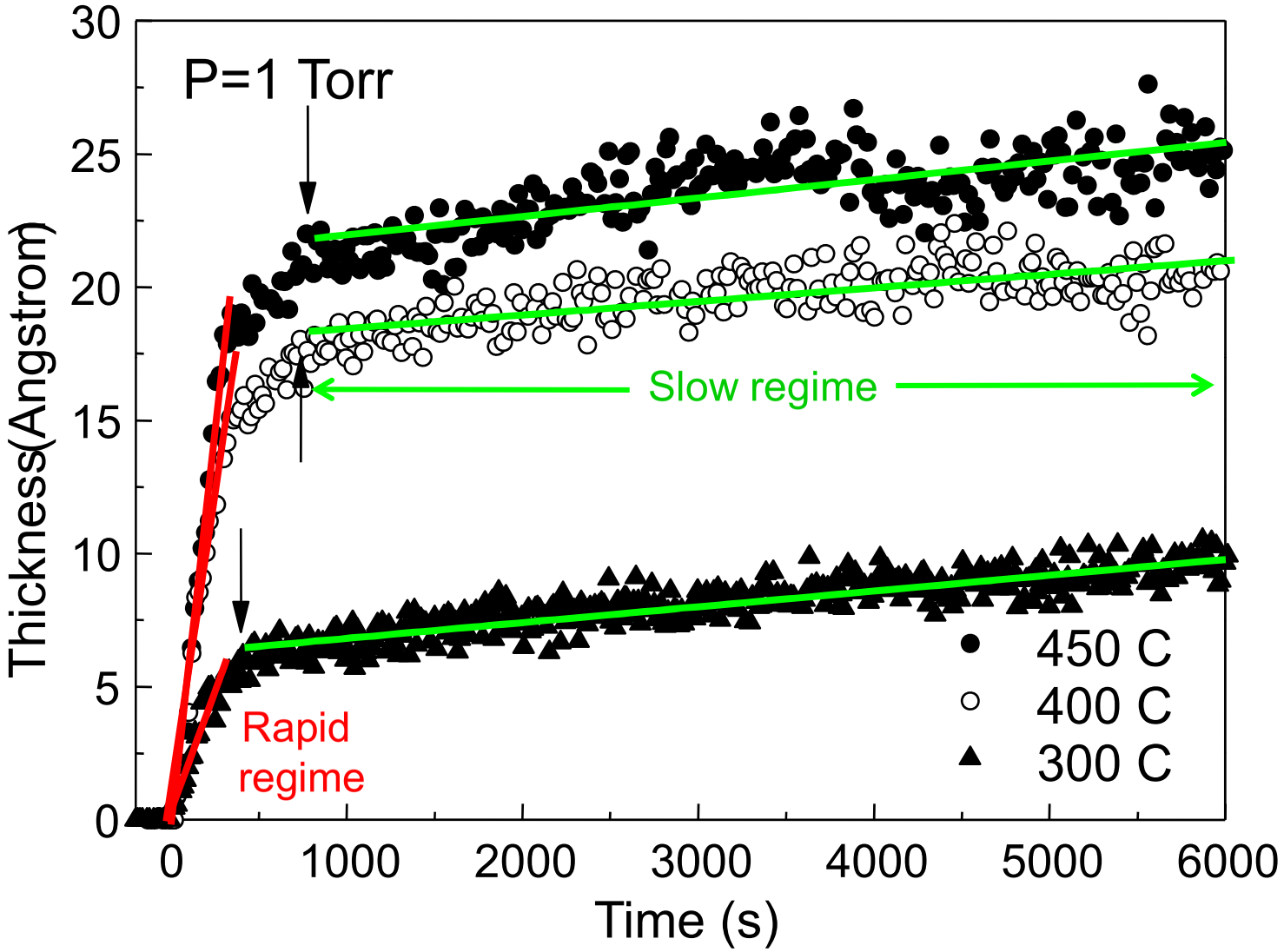

Fig. 27